crystals

MDPI

Article

Complex Coacervates: From Polyelectrolyte Solutions to Multifunctional Hydrogels for Bioinspired Crystallization

Dominik Gruber [1], Cristina Ruiz-Agudo [1,*], Ashit Rao [2], Simon Pasler [1], Helmut Cölfen [1,†] and Elena V. Sturm [1,3,*]

[1] Physical Chemistry, Department of Chemistry, University of Konstanz, Universitätsstr. 10, 78547 Konstanz, Germany; dominik.gruber@uni-konstanz.de (D.G.); paslersi@gmx.de (S.P.)
[2] Faculty of Science and Technology, University of Twente, 7500 AE Enschede, The Netherlands; a.r.rao@utwente.nl
[3] Department of Earth and Environmental Sciences, Section of Crystallography, Center for NanoScience, Geobio-Center, Ludwig Maximilian University of Munich (LMU), Theresienstr. 41C, 80333 Munich, Germany
* Correspondence: cristina.ruiz-agudo@uni-konstanz.de (C.R.-A.); sturm.elena@lmu.de (E.V.S.)
† Deceased author.

Abstract: Hydrogels represent multifarious functional materials due to their diverse ranges of applicability and physicochemical properties. The complex coacervation of polyacrylate and calcium ions or polyamines with phosphates has been uncovered to be a fascinating approach to synthesizing of multifunctional physically crosslinked hydrogels. To obtain this wide range of properties, the synthesis pathway is of great importance. For this purpose, we investigated the entire mechanism of calcium/polyacrylate, as well as phosphate/polyamine coacervation, starting from early dynamic ion complexation by the polymers, through the determination of the phase boundary and droplet formation, up to the growth and formation of thermodynamically stable macroscopic coacervate hydrogels. By varying the synthesis procedure, injectable hydrogels, as well as plastic coacervates, are presented, which cover a viscosity range of three orders of magnitude. Furthermore, the high calcium content of the calcium/polyacrylate coacervate (~19 wt.%) enables the usage of those coacervates as an ions reservoir for the formation of amorphous and crystalline calcium-containing salts like calcium carbonates and calcium phosphates. The exceptional properties of the coacervates obtained here, such as thermodynamic stability, viscosity/plasticity, resistance to acids, and adhesive strength, combined with the straightforward synthesis and the character of an ions reservoir, open a promising field of bioinspired composite materials for osteology and dentistry.

Keywords: hydrogel; polyacrylate; polyamine; calcium phosphate; calcium carbonate; dentistry

Citation: Gruber, D.; Ruiz-Agudo, C.; Rao, A.; Pasler, S.; Cölfen, H.; Sturm, E.V. Complex Coacervates: From Polyelectrolyte Solutions to Multifunctional Hydrogels for Bioinspired Crystallization. *Crystals* **2024**, *14*, 959. https://doi.org/10.3390/cryst14110959

Academic Editor: Zhaohui Li

Received: 11 October 2024
Revised: 28 October 2024
Accepted: 31 October 2024
Published: 2 November 2024

1. Introduction

Hydrogels are a three-dimensional network of chemically or physically crosslinked polymers that can swell in water while retaining their integrity. They exhibit outstanding properties, which are achieved by tuning the synthesis route and the crosslinking mechanism [1–3]. For this reason, synthetic hydrogels can be implemented in various fields like water treatment [4], adhesives [5,6], or medical applications such as drug carriers [7], tissue scaffolds [8,9], or injectable implants [10]. The extensive set of properties of hydrogel materials is often obtained through chemical crosslinking, which, however, limits their possible field of applications [11]. In addition to covalently crosslinked hydrogels, physical hydrogels, crosslinked by non-covalent interactions under mild conditions, are particularly important [2,10–12]. The non-covalent bonds of physical hydrogels are individually less stable than covalent chemical bonds, whereas combining different non-covalent interactions, such as hydrogen bonds, electrostatic, hydrophobic, and/or van der Waals interactions can achieve synergistic effects [11]. Non-covalent interactions are also a frequently used approach by nature to produce superb materials [13]. For instance, the sand castle worm

glues mineral particles (shells, sand etc.) with a complex adhesive consisting of three highly polar proteins, which are mainly crosslinked via electrostatic interactions, to build a protective hybrid organic–inorganic tunnel [14,15]. The crosslinking of oppositely charged macromolecules, like the mentioned proteins, polyelectrolytes, colloids, or surfactants, often results in a phase separation event—complex coacervation [16–18].

Coacervation depicts an electrostatically-induced liquid–liquid phase separation, resulting in a dense and polyelectrolyte-rich liquid phase termed 'coacervate' [17,18]. This process is widely used in the food industry [19,20], as a model for protocell assemblies [21–23] as well as for the encapsulation of growth factors [24], proteins [25], and genes (DNA) [26]. One distinct example is presented in the coacervation of polyamines (i.e., poly(allylamine hydrochloride), PAH) and phosphates yielding pH and mechanically stable coacervates, which have been suggested as adhesives or for carrying third-party components [27–31]. In addition, our group recently showed the potential of these coacervates as ion reservoirs for subsequent precipitation reactions to calcium phosphates (CaP) [32]. Lauth et al. introduced a "mineralized" calcium-containing coacervate for the pH-responsive encapsulation and delivery of biomolecules [33]. Here, the coacervation occurs via the complexation of calcium ions by polyacrylates (PAs) [33–36]. The complex binding mechanism of calcium ions by PA, the resulting changes of the polymer chain conformation, and finally, their precipitation have been investigated extensively [37–39]. However, most studies focused mainly on high molecular weight (M_W) Pas [37–43].

In the last few decades, the successful conversion of those calcium/polyacrylate coacervate emulsions to amorphous calcium carbonate (ACC) [33–35] and phosphate (ACP) [44] was realized. Nevertheless, the main drawback of the emulsions is their low colloidal stability, which results in their fast growth, coalescence, and/or fusion, yielding to the formation of macroscopic coacervate hydrogels [35,45]. A recent study of our group showed that the rheological behavior of these precipitated hydrogels is tunable by varying the M_W of the used polyacrylic acid [46]. Lower molecular weight polyacrylic acids (<50 kDa) resulted in hydrogels that evinced a liquid-like character [46]. These types of coacervates are highly advantageous for the infiltration of confined spaces. Therefore, more profound insights into the distinct steps of the formation mechanism should be very beneficial for controlling their properties. To the best of our knowledge, the multifunctional properties of calcium-containing coacervate hydrogels with such a liquid-like character and thermodynamic stability have never been investigated in detail nor systematically considered for possible applications. Furthermore, gaining fundamental knowledge about the precipitation mechanism of these coacervates is a special concern when controlling the properties of the emergent material [3].

Here, we report the formation mechanism of the calcium-containing and phosphate-containing coacervates enabling us to draw intriguing parallels between the contrary systems. We shed light on the initial and intermediate stages of the formation process, starting from relatively low molecular weight polymer solutions, through ion complexation, phase boundary, and emulsion formation, up to development of multifunctional physical hydrogels with various application prospects.

2. Materials and Methods

2.1. Chemicals

Polyacrylate sodium salt (PA-Na, $M_W \approx 15$ kDa, 35 wt.% aq. solution), polyacrylic acid ($M_W \approx 100$ kDa, 35 wt.% aq. solution), $CaCl_2 \cdot 2H_2O$ (≥99%), $(NH_4)_2HPO_4$ (≥98%), 3-(trimethylsilyl)propionic-2,2,3,3-d_4 acid sodium salt (TMSPA, 98 at.% D), rhodamine B, methylene blue, NaOH (0.1 M and 1 M), HCl (0.1 M, 1 M and 37%), 3-(N-morpholino)propanesulfonic acid (MOPS ≥99.5%), and sodium tetraborate decahydrate ($Na_2B_4O_7 \cdot 10\ H_2O$, ≥99.5%) were purchased from Merck.(Darmstadt, Germany) $NaHCO_3$ (≥99%), $(NH_4)_2SO_4$ (≥99.5%) and $BaCl_2 \cdot 2H_2O$ (>99%) were obtained from Carl Roth (Karlsruhe, Germany). Poly(allylamine hydrochloride) (PAH, M_W = 15 kDa, 15% aq. solution) was obtained from Polysciences (Hirschberg an der Bergstrasse, Germany). D_2O (99.95%) was purchased from Deutero

(Kastellaun, Germany). All chemicals were used without further purification. All syntheses were conducted and all solutions were prepared with double deionized water (Merck, Millipore, (Darmstadt, Germany) 18.2 MΩcm) [3].

2.2. Titration Experiments

All titration experiments were conducted using the auto-titration setup Tiamo (Metrohm) equipped with an Optrode (λ = 590 nm), a pH electrode (flat membrane, Metrohm), and a calcium-ion selective electrode (Ca-ISE, Metrohm). The Ca-ISE was calibrated by titrating the $CaCl_2$ solution to water. The concentrations of the PA were always calculated for the sodium acrylate subunits. For the evaluation of the binding capacity of PA, 10 mL of a $CaCl_2$ solution (4 mM, pH 9) was added (50 µL/min) to a stirred PA solution (40 g, 50 mg/L, pH 9). For the investigation of the droplet formation, the $CaCl_2$ solution (50 mM) was added (1 mL/min, unless otherwise specified) to a stirred PA solution (40 g, 10 g/L, pH 9) to reach the mentioned Ca^{2+}/COO^- ratios. For the NMR experiments, the titrations were conducted using the same parameters as for the droplet formation experiments but using a PA solution with 18% (*v*/*v*) D_2O [3].

2.3. Coacervate Syntheses

For the investigation of the pseudo-phase diagram, two different synthesis approaches were used due to the wide concentration ranges. For low PA concentrations (≤10 g/L), 15 mL of a $CaCl_2$ solution (200 mM, pH given in Figure S10) was added quickly within some seconds to a vigorously stirred PA solution (15 mL, pH and concentration given in Figure S10). For the higher PA concentrations (>10 g/L), 1 mL of a 5 M $CaCl_2$ solution was added quickly to 1 mL of the PA solution. The samples were centrifuged afterwards to collect the coacervate hydrogel. For the confocal Raman microscopy investigations, a 200 mM $CaCl_2$ solution was added to 120 µL of the PA solution (100 g/L, pH 9) to reach the given r_{add} and centrifuged to obtain the hydrogel. The macroscopic coacervate hydrogels (low molecular weight coacervate (LMC), high molecular weight coacervate (HMC), and lowest ratio coacervate (LRC)) for the rheological measurements and the investigation of the properties were synthesized by adding a $CaCl_2$ solution (200 mM) quickly in one go to a vigorously stirred PA solution (12 mL, 100 g/L, pH 9) to reach the given r_{add}. Afterwards, the turbid mixtures were stirred for 5 min, whereby the hydrogel was sediment. If possible, the supernatant was discarded and each hydrogel was extensively washed three times with 40 mL water each. For the investigation of the self-healing, ~70 mM of rhodamine B or methylene blue was added to both reactant solutions prior to the synthesis for coloring purposes. The Ba^{2+}/PA coacervate was prepared by adding 720 mL of the $BaCl_2$ solution (100 mM, pH 7, ~40 mL/min) to a vigorously stirred PA solution (108 mL, 100 g/L, pH 9). The obtained hydrogel was washed three times with 400 mL water each. A small part of each coacervate was freeze-dried to investigate the coacervate powders (TGA, EDX, ATR-FTIR) [3].

2.4. Crystallization Experiments

The coacervates were filled in 1 mm thick templates, prepared by cutting a 2 × 2 cm square in a silicon mat in which a hole with a diameter of 11 mm was blanked out (Figure S20). This silicon mat was glued to a glass substrate by using a silicon grease. The coacervate was filled in the reservoir and straightened with a coverslip to produce a smooth and even surface. The filled templates were placed in 20 mL of the crystallization-inducing solutions. The formation of $CaCO_3$ took place over 20 d in a $NaHCO_3$ solution (200 mM, pH 10). The hydroxyapatite was crystallized within 14 d in a $(NH_4)_2HPO_4$ buffer (260 mM, pH 9) whereas the $BaSO_4$ was obtained after 1 h in 130 mM $(NH_4)_2SO_4$ solution at pH 7.4. After the formation of inorganic phases, the samples were washed carefully with water and dried at 37 °C [3].

2.5. Characterization of Materials

Thermogravimetric analysis (TGA) measurements were conducted on an STA 449F3 Jupiter from Netsch (Selb, Germany) under air atmosphere from 25 to 1000 °C using a heating rate of 10 K/min. The attenuated total reflection Fourier transform infrared spectroscopy (ATR-FTIR) analyses were conducted on a Perkin Elmer (Rodgau, Germany) Spectrum spectrometer. Scanning electron microscopy (SEM) images were recorded on a Zeiss Gemini 500 with an energy dispersive X-ray (EDX) detector (Oxford Ultim Max 100 (Oxford Instruments, High Wycombe, UK)). X-ray diffraction (XRD) studies were performed with a D8 Discover X-ray diffractometer (Bruker (Karlsruhe, Germany), Cu-Kα radiation) with a VANTEC-500 detector from Bruker. For the investigation of the droplet sizes, dynamic light scattering (DLS) measurements were conducted using a Zetasizer Nano from Malvern (Worcestershire, United Kingdom). The same setup was used for the ζ-potential measurements. The molecular weights of the used polyacrylate and polyacrylic acid were determined by gel permeation chromatography (GPC) equipped with a hydroxylated polymethacrylate column, an UV (λ = 260 nm), and a refractive index detector. The setup was calibrated by using sodium polyacrylate standards. The measurements were conducted using a 10 mM phosphate buffer as mobile phase with a flow rate of 0.8 mL/min at 35 °C. The initial PA concentration was 10 g/L whereby 0.1 mL was injected. Isothermal titration calorimetry (ITC) measurements were performed with a MicroCal VP-ITC (Malvern (Worcestershire, United Kingdom)). The data was analyzed and treated with the program NITPIC, GUSSI (University of Texas), and ITCsy (sedphat). The rheological behavior of the coacervates was investigated using a DHR2 rheometer (TA instruments (Eschborn, Germany)) with parallel-plate geometry (40 mm) in oscillation mode at a fixed strain (0.2%). The measurements were performed for the 0.01–100 s^{-1} frequency range at 25 °C. Confocal Raman microscopy experiments were conducted with a WiTec alpha 300R (Ulm, Germany) setup equipped with a 523 nm laser. A spectral resolution of 2.3 cm^{-1} was reached by a grating of 600 g/mm. A CCD camera (Andor Newton (Oxford Instruments, High Wycombe, UK), 16 µm pixel size, 1600 × 2000 pixels) and a 50× objective from Zeiss EC Epipna (numerical aperture = 0.75) (Oberkochen, Germany) were used. Raman maps were generated by integrating the spectral regions of interest for every pixel (cf. caption Figure S18). To evaluate the water content, the considered regions (white frames in Figure S18A) had a size of 5 × 10 (50 spectra) each. The baseline correction of the spectral data sets was performed using the Witec ProjectFIVE software (WITec GmbH, Ulm, Germany). Density measurements (Table S1) for the calculation of the PA concentrations (by weighing) were made with a density meter DMA 5000M (Anton Paar (Graz, Austria)). Furthermore, the Density Meter was equipped with a Microviscometer Louis 2000 ME (Anton Paar) for the determination of the solution viscosities (Table S1), which was needed for the calculations of the hydrodynamic radii based on the ^{1}H-PFG-STE NMR studies. The one-dimensional ^{1}H-NMR experiments and ^{13}C-NMR measurements (Figure S3) were conducted on a Bruker Avance Neo 800. For the measurements, which were conducted at 298 K, 1 mL of each sample obtained from the titration experiments described above, was filled into a 5 mm tube, whereby deuterated TMSPA was used as a reference for the proton signals. For the determination of the translational diffusion coefficient D, pulsed field gradient stimulated echo (PFG-STE) NMR experiments were conducted on a Bruker Avance III 600. Therefore, the gradient pulse time for de- and rephasing along the z-axis was set to δ = 4 ms. Furthermore, the diffusion time was set to Δ = 200 ms and the gradient field pulse G ranged between 1% and 95% to generate 22 spectra slices (proton) for further analysis. The gradients were calibrated as described elsewhere [47]. The raw data were processed using the TOPSPIN 3.5 software (Bruker, Karlsruhe, Germany), and the ORIGIN 2024 software (OriginLab Corporation) was applied to fit the data. By fitting the following, modified, Stejskal-Tanner equation [48,49], the diffusion coefficients were obtained:

$$ln\left(\frac{A}{A_0}\right) = -D\cdot(G\cdot\gamma\cdot\delta)^2\cdot\left(\frac{2}{\pi}\right)^2\cdot\left(\Delta-\frac{\delta}{3}\right)$$

where (A/A_0) is the ratio of the signal intensity with and without the gradient, G is the gradient field strength, D is the diffusion coefficient, δ is the duration of the applied gradient application, Δ is the diffusion time, and γ is the gyromagnetic ratio of ^{1}H. The Stejskal-Tanner equation has a general character, which was defined for a rectangular gradient [49]. Since a sinusoidal gradient was used in this study, the term $(2/\pi)^2$ must be considered for G in data regression. By plotting the left part of the equation against $(G\gamma\delta)^2(2/\pi)^2(\Delta - \delta/3)$, a linear relation is obtained whereby the slope reflects the diffusion coefficient [3,50].

3. Results and Discussion

The first part of the study is focused on the calcium/polyacrylate coacervate formation mechanism, which is compared to the mechanism of phosphate/polyamine coacervates unraveled in the second part, prior to investigating the macroscopic properties of the calcium-containing coacervates.

For examining calcium ion complexation by polyacrylates, the deprotonation level of the polymer [51], which is reflected in the pKa value, as well as the M_W [39,52], and the polydispersity (PDI) [46] play pivotal roles. The pKa value of the PA used in this study (commercially obtained) was determined to be 4.28 (Figure S1A). The molecular weight was measured via gel permeation chromatography and amounted to M_W = 19,500 g/mol with a high PDI of 4.9 (Figure S1B).

3.1. Calcium Complexation by Polyacrylate

The thermodynamic properties of the calcium complexation by PA were studied by isothermal titration calorimetry (ITC), indicating an endothermic complexation reaction (Figure S2A). Based on of the binding curve (Figure S2B), thermodynamic variables were calculated ($\Delta G = -26.7$ kJ/mol, $\Delta H = 7.9$ kJ/mol, $-T\Delta S = -34.6$ kJ/mol, T = 298 K), which are in good agreement with previous studies [37,53] elucidating an entropically-driven complexation, which is based on the release of water molecules from the ion hydration shells [37]. The complexation of the Ca^{2+} ions can pass through several intermediate binding stages before reaching the most stable bidentate chelation of two carboxylic groups per Ca^{2+} ion [54]. Those changes in calcium coordination require a dynamic calcium binding, which was confirmed by nuclear magnetic resonance (NMR) spectroscopy. The one-dimensional ^{1}H-NMR spectra of the PA-Na as well as for different calcium-to-carboxylate ratios ($r_{add} = Ca^{2+}/COO^-$) are shown in Figure 1. With an increasing r_{add}, the resonance signals of both, the methylene protons ($\delta \approx 1.5$ ppm) and the methine protons ($\delta \approx 2.1$ ppm) of the acrylate subunits were shifted to higher chemical shifts, compared to the PA-Na solution. The shifts were more pronounced for the signals of the methine protons due to the closer location to the calcium-binding side. In addition, the same effect was observed in ^{13}C-NMR spectra characterizing the carboxylate carbon of the acrylate subunits (Figure S3). The shift of the resonance signals indicated the dynamic character of PA-Ca^{2+} binding, which can be categorized as a fast exchange process on the NMR timescale. Therefore, the observed resonance signals report an average between unbound and bound states. If the calcium-binding had been a static complexation, a peak splitting would have been expected, which was related to separated bound and non-bound carboxylate stages [3]. The reaction mixture for a Ca^{2+}/COO^- ratio of $r_{add} = 0.387$ was turbid, indicating that the phase separation occurred and coacervate droplets formed. Intriguingly, no peak splitting was observed for this phase-separated emulsion, which is discussed in the section below. This result indicates a dynamic calcium exchange between the coacervate phase and the solution. The dynamic character of the calcium binding is responsible for the properties of the coacervate hydrogels, which are discussed in the application section. Furthermore, the shape of the proton resonance signals changed by comparing $r_{add} = 0.094$ and $r_{add} = 0.189$, which could be due to variations in the binding mechanism in between these two ratios [54].

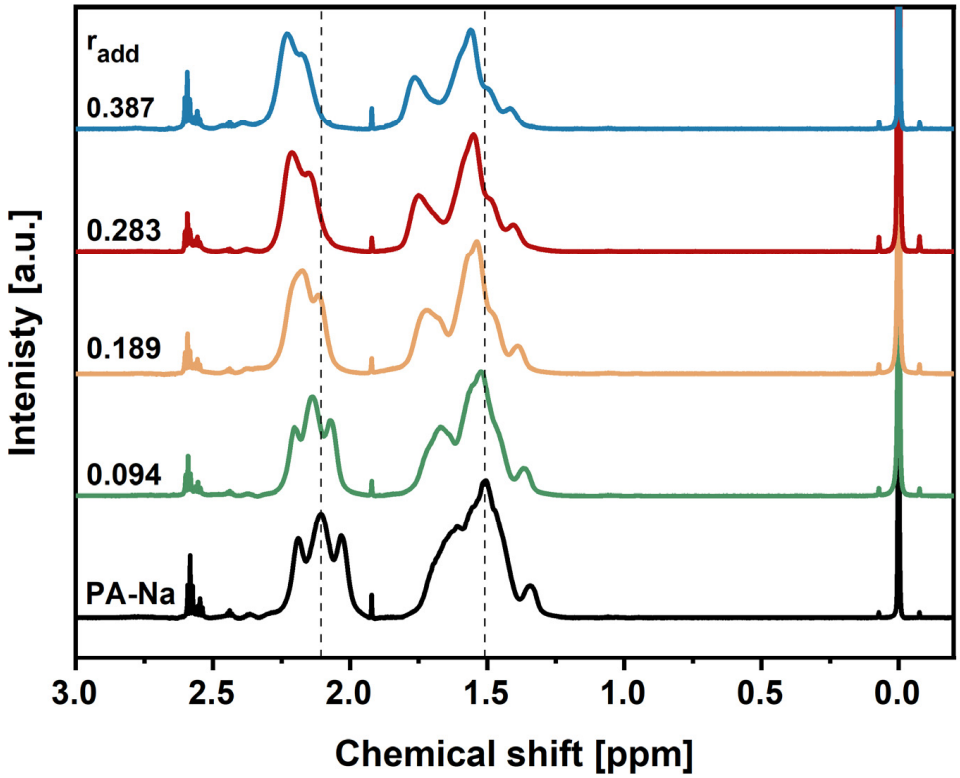

Figure 1. One-dimensional ^{1}H-NMR spectra acquired for pure PA-Na and for different Ca^{2+}/COO^{-} ratios (r_{add}). These measurements were referenced to deuterated TMSPA (3-(trimethylsilyl)propionic acid sodium salt, 0 ppm). A ratio of r_{add} = 0.387 corresponded to a turbid, phase-separated mixture. The distinct narrow resonance signals (~1.92 ppm and ~2.6 ppm) indicate molecular impurities of the commercially obtained PA-Na, which was used without further purification.

Potentiometric titration experiments were conducted to quantitatively investigate the complexation of Ca^{2+} ions by PA by titrating a $CaCl_2$ solution to a PA solution. The free calcium was monitored in situ during the addition of a $CaCl_2$ solution by using a calcium-ion selective electrode (Ca-ISE) and translating the calcium potentials to free calcium-ion concentration/activity (Figure 2, solid black line). The dotted black line displays the theoretical value of added calcium. Initially, the added Ca^{2+} ions are bound completely by the PA, which was indicated by no free calcium ions being detected in the solution, until a Ca^{2+}/COO^{-} ratio of 0.175 was reached. It is noteworthy that the ratio of 0.175 lies in between the ratios in which the changes in the line shape of the resonance signals were observed in the one-dimensional ^{1}H-NMR experiments. We propose that those calcium ions content-dependent changes observed in the NMR spectra may be reconciled with the investigated changes of Ca^{2+} coordination and possible intermediate binding states [54]. By the further addition of Ca^{2+} ions, a maximum binding capacity of the PA via an ion exchange mechanism was determined to a Ca^{2+}/COO^{-} ratio (r_{bound}) of 0.331 by extrapolating the calcium curve to the x-axis (Figure 2, red dotted line) [55]. Due to the low polymer concentration, a further increase in the calcium concentration is not inducing a coacervation process [3,56].

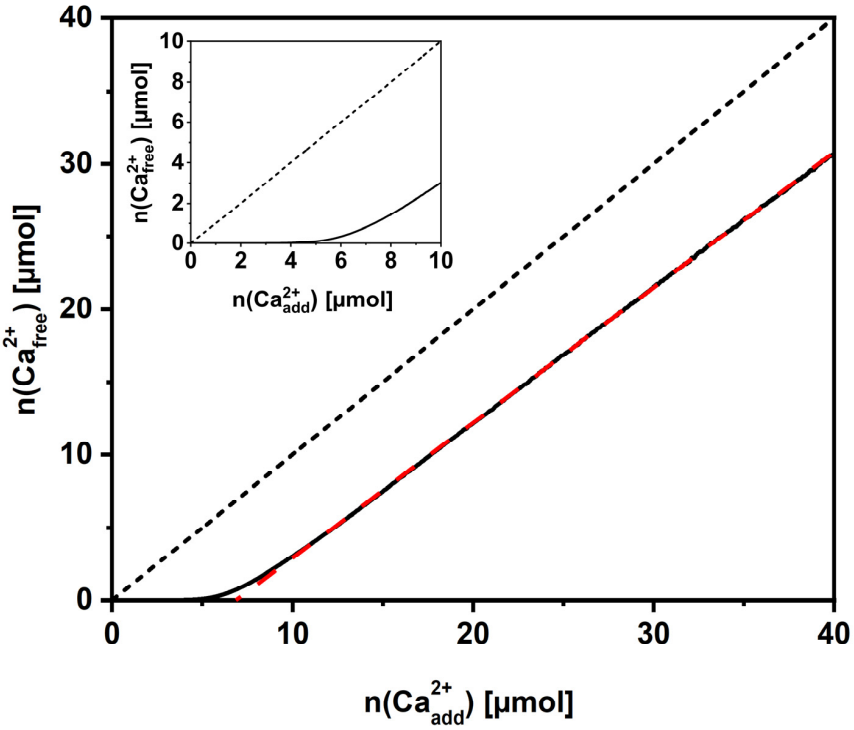

Figure 2. The calcium binding capacity of PA (20.8 µmol) was determined by monitoring the free calcium (solid line) during the titration of a 4 mM $CaCl_2$ solution and extrapolating to the x-axis (red dotted line). The dotted black line depicts the theoretical evolution of the Ca^{2+} concentration during the titration experiments under the assumption that all the calcium added remains free in the solution. The zoom-in highlights the region of a complete complexation of added Ca^{2+} ions by PA.

3.2. Phase Separation—Coacervation's Mechanism

The above-discussed calcium complexation experiments were conducted using low PA concentrations to investigate the ratio of complete calcium complexation as well as the maximum binding capacity of the PA by the ion-complexation mechanism. This represents the first step in the formation process of the coacervate gels. To investigate the phase separation and the evolution of the coacervate emulsions, the concentration of PA was increased by a factor of 200 (to 10 g/L), whereby also the addition speed and the concentration of the $CaCl_2$ were increased (see Experimental Section 2.3 for details). During the formation of the droplet phase, various important questions arise; for instance, at which Ca^{2+}/COO^- ratio the phase separation occurs, what the formation mechanism is, and how the stability of the coacervate emulsion can be achieved.

To gain more insights into the formation mechanism of the coacervates, a combination of potentiometric titration experiments was used, whereby the transmittance, the pH, and the free calcium ions concentration (activity) were monitored in situ during the addition of the $CaCl_2$ to the PA solution. Various final Ca^{2+}/COO^- ratios (r_{add}) were studied to identify the optimal conditions yielding stable coacervates.

One exemplary measurement for the addition of Ca^{2+} ions to reach $r_{add} = 0.387$, which induced phase separation, is shown in Figure S4 and further discussed in the supporting information. The drop in the transmittance curve indicated the formation of the coacervate phase. Like the Ca^{2+} binding experiments conducted at lower PA concentrations (Figure 2), no free calcium ions are detected in the solution during the first ~900 s. This first regime for the free Ca^{2+} was followed by a linear increase in the free calcium ions in the solution. After the Ca^{2+} addition was completed, the growth of the coacervate droplets was confirmed by dynamic light scattering (DLS) analyses from aliquots taken during the potentiometric measurements (Figure S5). The size of the droplets and the emulsion stability is of particular interest for possible applications, such as ions reservoir for precipitation reactions [34,35,44]

or micro- [33] and nanocarriers [57]. We concluded that the emulsion stability was increased up to days by (a) mitigating diffusive and mixing processes, i.e., by avoiding any stirring after the $CaCl_2$ addition was completed, and (b) by maintaining r_{add} close to approaching the critical ratio r_{crit} for phase boundary (Figure S6). Consequently, the central question, that needs to be unraveled is the precise value of r_{crit}, enabling the investigation of the phase boundary's locus for the system examined here. Determining this phase boundary is essential for engineering the coacervate stability and physicochemical properties toward potential applications such as infiltrates in restructuration, dentistry, or osteology.

Accordingly, for demarcating the phase boundary, the combined titration experiments were conducted, lowering the added amount of $CaCl_2$ progressively from r_{add} = 0.387 (Figure S4) to 0.377 (Figure S7A, discussed in the supporting information) and finally to 0.375 (Figure 3A). It should be noted that a fraction of the added calcium ions was not bound and, in turn, measured via the Ca-ISE. Therefore, the added Ca^{2+}/COO^- ratio (r_{add} = 0.375) can be corrected to a bound ratio (r_{bound}), which was 0.349 when the phase separation occurred. Interestingly, the higher capability of Ca^{2+} coordination, compared to lower concentrations and addition rates (Figure 2, r_{bound} = 0.331), indicates that a faster Ca^{2+} addition results in higher binding ratios [58], which is later pushed to the limit in the macroscopic coacervate section. However, for the sake of clarity and the comparison with the literature, the ratio of the added Ca^{2+} (r_{add}) is given for further experiments. The transmittance curve showed only a slight drop after an induction time of more than 1 h (Figure 3A).

This drop in transmittance marked the phase separation and is most likely caused by a dynamic rearrangement of the Ca^{2+}/COO^- bonds as well as transitions in the coordination structure and solvation. DLS measurements after the Ca^{2+} addition was completed but before the transmittance dropped point out the existence of a small species with a hydrodynamic diameter (d_H) of 6–7 nm (Figure 3B, black). The signal intensity of this species decreased within 20 h, and larger droplets of several hundreds of nm rose within the same time (Figure 3B, colored). Furthermore, the occurrence of an initial small species, which was separated by a significant size gap from the larger species, suggested that the small droplets grew mainly due to coalescence and fusion processes and less likely due to ripening. The detected 6–7 nm species could be single PA chains that bind Ca^{2+} ions by intramolecular binding processes, which in a later stage develop intermolecular crosslinks yielding larger coacervate droplets. A further indication of this assumption is that the small species are in the same size range as single PA chains (with comparable M_W) [38]. In addition, no large species were observed for a further lowering of r_{add} (0.373, results not shown). Therefore, the phase boundary for the coacervate formation was determined to a critical addition ratio of r_{crit} = 0.375. It should be mentioned, that DLS measurements of a pure PA solution were not feasible due to the low scattering intensity of the low molecular weight polymer chains.

Unraveling the nature of the first species (d_H = 6–7 nm) formed during the calcium ions addition may be relevant for exerting control over their aggregation process, which leads to the formation of the droplet phase. If these initial species are composed of single PA chains, which bind Ca^{2+} ions intramolecularly, the hydrophobicity of the polymer will increase due to the screening of the negative charges by the Ca^{2+} ions, as predicted in former studies [37,41,52]. The ζ-potential can estimate the hydrophobicity of the complexes' surface due to the charge compensation of the PA, induced by the Ca^{2+} coordination, which would result in a less negative value than the pure PA solution (−48 mV at pH 7.4). The measured ζ-potentials for different r_{add} are displayed in Figure 4A. The measurements were conducted 10 min after the addition of the $CaCl_2$ was completed to ensure the detection of the major species. With an increasing r_{add}, the negative ζ-potential decreased to a minimum value of −8 mV for r_{add} = 0.375 and increased again for higher ratios to an almost constant value of −21 mV. This minimum at r_{add} = 0.375, for which also the small species was detected by DLS, points to the hypothesis that the intramolecularly coordinated Ca^{2+} ions increased the hydrophobicity of the polymer chains, whereby a coil-to-globule transition would be induced as described in previous studies [52,59]. The

increasing negative ζ-potential to −21 mV for increasing r_{add}, indicates an electrostatic stabilization of the coacervate droplets. Furthermore, the Ca^{2+}-induced phase separation of polyacrylates was described by Huber et al. [39–41,60] In these studies, the phase boundary, and, therefore, the critical calcium ions concentration were quantified for higher molecular weight PA (30 times higher) and lower concentrations (10 times lower) compared to our studies [39]. Nevertheless, we extrapolated the phase boundary established by the group of Huber to the concentration region of our experiments. Astonishingly, the critical ratio predicted by the extrapolated phase boundary was 0.391, which is remarkably close to our investigations. The slightly higher extrapolated value is most likely caused by the fact that a higher Ca^{2+}/COO^{-} ratio must be achieved for higher molecular weight PA to induce phase separation [39].

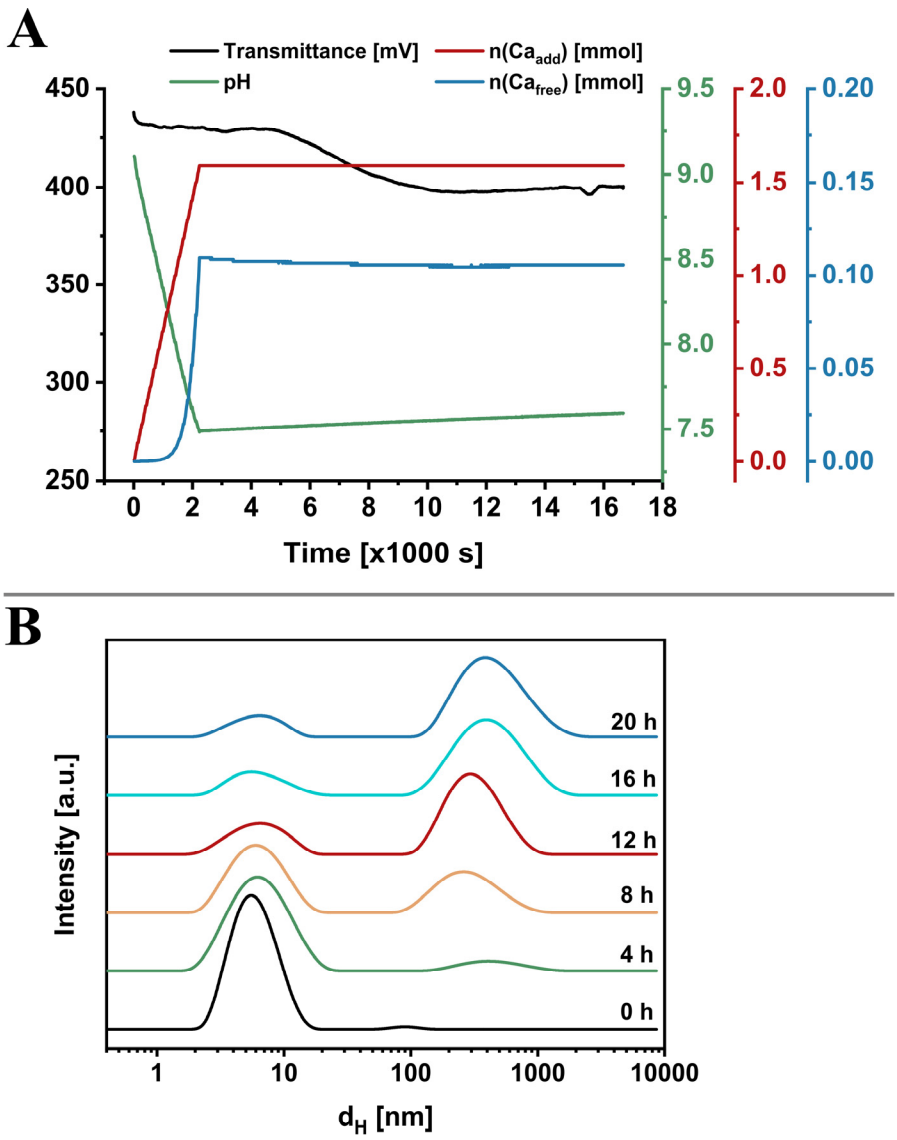

Figure 3. (**A**) Potentiometric titration experiment for the addition of $CaCl_2$ to reach r_{add} = 0.375. After the addition was completed, the transmittance slightly decreased after an induction time of more than 1 h. (**B**) Time-dependent DLS measurements for the calcium addition to reach r_{add} = 0.375. Directly after the addition was completed (black) a small species of d_H = 6–7 nm was detected. The intensity of the small species decreased within 20 h whereas a larger species grew (~250–400 nm).

For the further investigation of the coil shrinking during the addition of Ca^{2+} ions, the ^1H pulsed field gradient stimulated echo (PFG-STE) NMR experiments were conducted

enabling the determination of diffusion coefficients (D) of the polymer chains [49,50,61]. In the pure PA solution at pH 9 (r_{add} = 0), the polymer adopts the conformation of a highly extended chain due to the repulsion of the negatively charged acrylate subunits [39]. This stretched conformation is reflected in the smallest diffusion coefficient determined here (Figure 4B). The obtained diffusion coefficients for the calcium-containing samples increased with an increasing r_{add} and followed a quadratic function untill the phase separation (r_{add} < 0.377) occurred (Figure 4B) indicating a decrease in the complex's size.

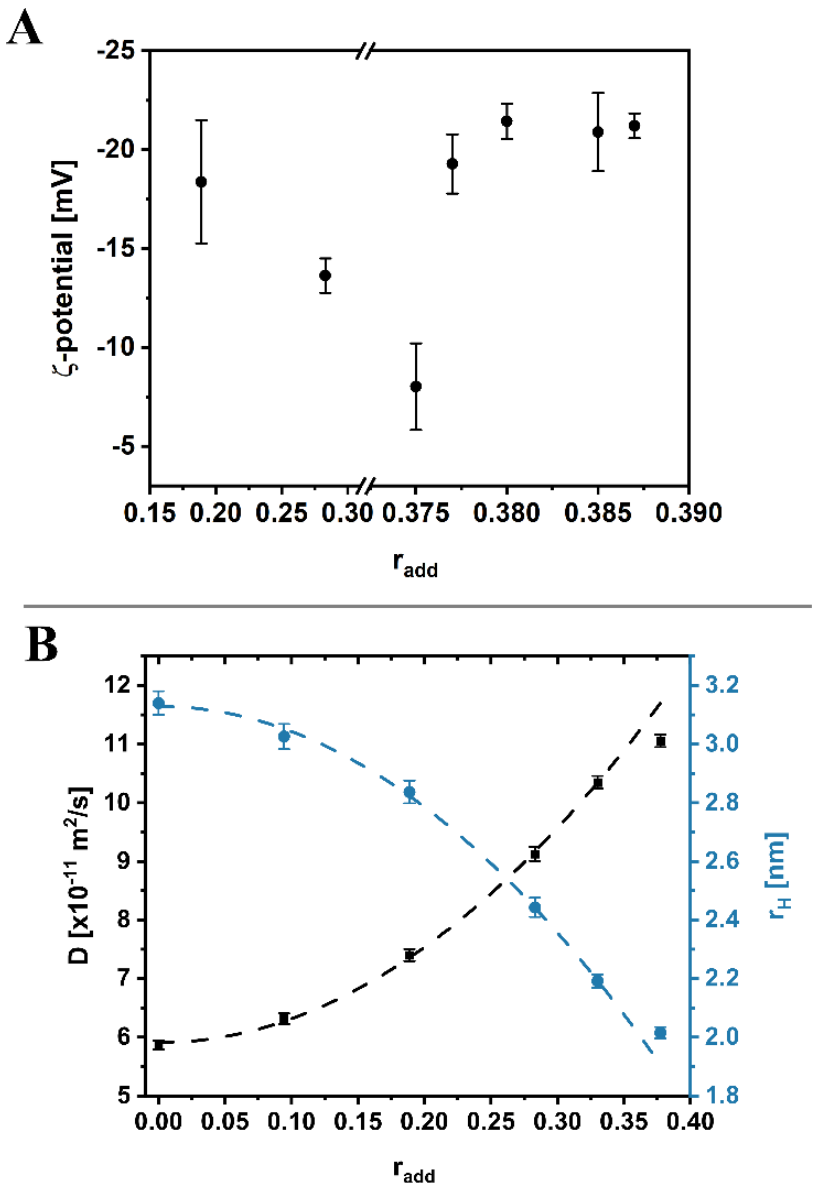

Figure 4. (**A**) ζ-potential measurements for different Ca^{2+}/COO^- ratios (r_{add}) show a decrease of the negative values with increasing r_{add} to reach a minimum at r_{add} = 0.375, which was determined to be the critical ratio for phase separation. (**B**) The diffusion coefficients (black squares) of the PA for different ratios of r_{add} were obtained by fitting the ^{1}H-PFG-STE NMR measurements using the Stejskal-Tanner equation [48,49,61]. The dotted line is a guide to the eyes elucidating the deviation of the sample with the highest r_{add}. The hydrodynamic radii r_H (blue circles) were calculated using the Stokes-Einstein equation, wherefore the viscosity of each sample was measured separately (Table S1) and deployed for the calculations.

The diffusion coefficient deviated from the quadratic growth function after the phase separation occurred (Figure 4B, r_{add} = 0.377). It should be noted that the measured D

values are averaged values that do not distinguish between dissolved PA chains and polymer chains within the dense coacervate droplets. While the addition of calcium ions is reflected in an increasing D due to the coil shrinking, the aggregation and precipitation of the globular structures counter this trend due to intermolecular crosslinks. However, according to the Stokes-Einstein equation, an increasing diffusion coefficient corresponds to a decreasing hydrodynamic radius (r_H) if the viscosity remains constant. The viscosities for all ratios investigated via ^{1}H-PFG-STE NMR were measured separately and considered in the calculations (Table S1). The calculated hydrodynamic radius of 3.15 nm for pure PA agrees with the previously reported radii of PA possessing comparable M_W [38]. Due to the calcium addition and the resulting screening of the repulsive charges of the PA, the single polymer chains shrunk. The measured r_H of 2.20 nm before the phase separation was slightly smaller than the size determined by DLS but still in good agreement. It should be noted that the pH-dependent conformational changes related to the pH decrease during the addition of the $CaCl_2$ solution can be excluded for the low molecular weight PA used in these studies [62].

The combination of ^{1}H-NMR, DLS, ζ-potential and ^{1}H PFG-STE NMR measurements unambiguously verified that in the first phase, single PA chains dynamically bind Ca^{2+} ions intramolecularly, which induces a screening of the negative charges of the PA (Figure 5) This results in coil shrinkage and, finally, in more hydrophobic globular structures. Those structures further aggregate at a critical ratio of 0.375 and crosslink intermolecularly [52,59,60,63]. Due to the crosslinking and, therefore, the rearrangement of the dynamic calcium binding, the dense coacervate droplets are electrostatically stabilized, which is indicated by highly negative values of the ζ-potential after the phase separation. At the later stage, the droplets of the coacervate emulsion coalesced and formed an adhesive macroscopic coacervate hydrogel [3].

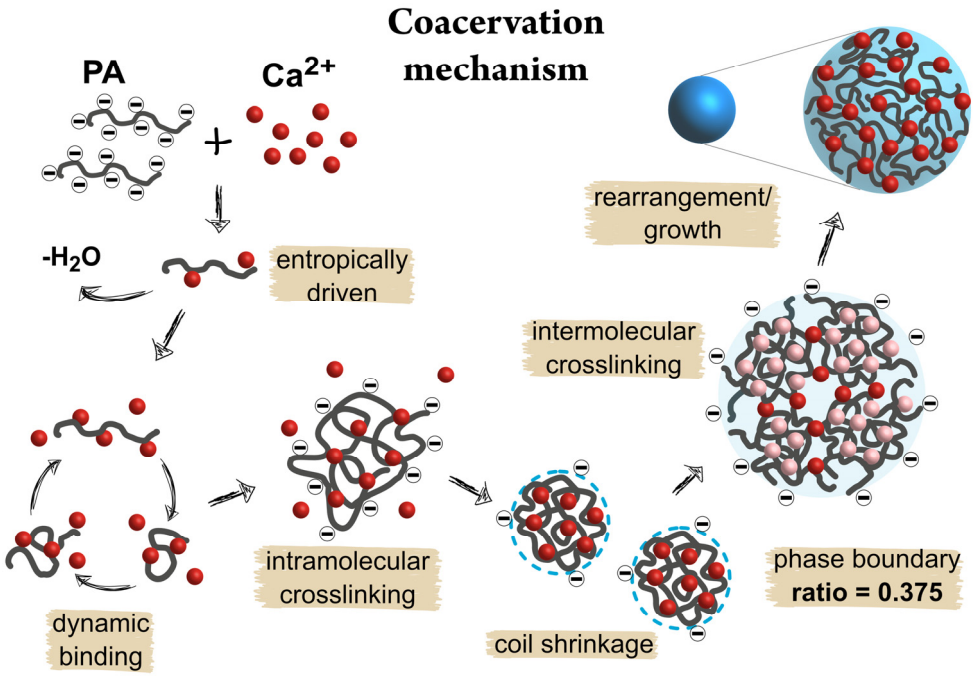

Figure 5. Illustration of the complete coacervation mechanism starting from the initial calcium complexation, including the dynamic intra- and intermolecular binding behavior, finally resulting in reaching the phase boundary's locus forming the coacervate electrostatically stabilized coacervate droplets.

3.3. PO_4^{3-}/PAH Coacervation Mechanism

With the knowledge about the coacervation mechanism for Ca^{2+}/PA coacervates, the question arose regarding whether the principles could be transferred to other systems, e.g.,

the coacervation of cationic poly(allylamine hydrochloride) (PAH) crosslinked by multivalent anions ((hydrogen)phosphate), which are further called cationic coacervates due to the cationic character of the structural polymer. These coacervates were recently uncovered as suitable phosphate reservoir for further reactions, e.g., the formation of different calcium phosphate phases [32]. A fundamental understanding of the coacervation mechanism would facilitate the tuning of coacervate properties towards multifunctional and versatile hydrogels. Cationic coacervation mechanisms might be even more sophisticated than the anionic counterpart (Ca^{2+}/PA coacervates vs. PO_4^{3-}/PAH coacervates). The intricacy is due to the fact that the electrostatic interaction based on the (de)protonation level of the PAH and phosphate is opposed. A high deprotonation (high pH) for the crosslinking phosphate units would be beneficial to maximize electrostatic interactions, whereas the protonation of the PAH needs to be high coincidently (low pH). The pH's sweet spot of both solutions (pH 3 for PAH and pH 7 for phosphate solution) enabling a sufficient coacervation was presented in detail in our recent study [32].

The first step toward coacervation is the complexation between phosphate and PAH, characterized by ITC, which evidenced an exothermic binding reaction (Figure S8A). The integration of the raw data (Figure S8B) revealed an enthalpy-driven complexation mechanism differing from the Ca^{2+}/PA system (endothermic process, entropy-driven association, see Figure S2).

^{1}H-PFG-STE NMR measurements were performed to study the polymer conformation of the PAH molecules (Figure 6A). In phosphate-free PAH solution (pH 5.5), the polymer chains were extended due to the electrostatic repulsion of the ammonium units since the PAH was completely protonated at values below pH 5.8 (Figure S9). The extended conformation is reflected in the smallest diffusion coefficient. For increasing r_{add}, the conformation changed from extended to smaller structures, which is reflected in a slowly increasing diffusion coefficient until a ratio of 0.334 was reached. Afterwards, the increase was steeper, which is proposed to be caused by the shrinkage of the coil-like structure, forming more globular structures. The dotted line in Figure 6A is a guide to the eyes but indicates an inflection point of the increasing D slightly above a ratio of 0.500, evidencing the phase separation's locus, as described for the Ca^{2+}/PA coacervate. The diffusion coefficients were transferred to hydrodynamic radii under consideration of the sample's viscosities (Table S1). The reason for the slight increase in r_H for r_{add} = 0.334 is most likely based on the significant changes in viscosity of the sample (Table S1) and is not related to the diffusion of the polymer since the measured diffusion coefficient followed an increase. However, the r_H of pure PAH was determined to be 3.8 nm, which is consistent with previously reported radii [64]. Shortly before the predicted phase separation occurred, the collapsed PAH molecules shrank to a size of 3.15 nm (r_{add} = 0.500). The observed shrinkage, in turn, is accompanied by the PAH's intramolecular crosslinking by phosphate ions, resulting in the screening of the positive charges. To confirm this hypothesis, ζ-potential measurements were performed in the region of the expected phase boundary's locus (Figure 6B). With an increasing r_{add}, the ζ-potential of the initial PAH solution (38 mV at pH 5.5) decreased, reaching a minimum of 8 mV at r_{add} = 0.502 and increasing again for higher ratios to an almost constant value of ~27 mV. The occurrence of a ζ-potential minimum and the deviation of the diffusion coefficient in the NMR studies at almost the same r_{add} solidifies the prediction about the location of the phase boundary.

DLS investigations were performed to precisely localize the critical ratio by varying the added phosphate to amine ratio progressively from r_{add} = 0.493 to 0.516 (Figure 6C). The lowest investigated ratio revealed the smallest species with a hydrodynamic diameter of 6–7 nm, whose signal exiguously broadened for a ratio of 0.502 with a slight evolution of larger sizes. This small species' d_H perfectly matched the size determined by NMR studies (r_H = 3.15 nm) shortly before phase separation occurred and was stated to be intramolecularly crosslinked single PAH molecules. After crossing the phase boundary (higher r_{add}), the small species' signal started to form a broad shoulder, indicating the formation of a larger species, which reached a size of d_H = 140 nm (r_{add} = 0.516).

These results unequivocally evince the similarity of the coacervation mechanism of the PO_4^{3-}/PAH and the Ca^{2+}/PA systems, even if the initial driving force for ion–polymer complexation (ITC results) is different. Identification and control over the essential synthesis parameters provide the possibility to tune coacervate properties for cationic and anionic systems. In the further course of this study, the focus is on justifying and evaluating the properties and possible purposes of macroscopic Ca^{2+}/PA coacervates since we already exemplified feasible applications of cationic coacervates in former studies [3,32].

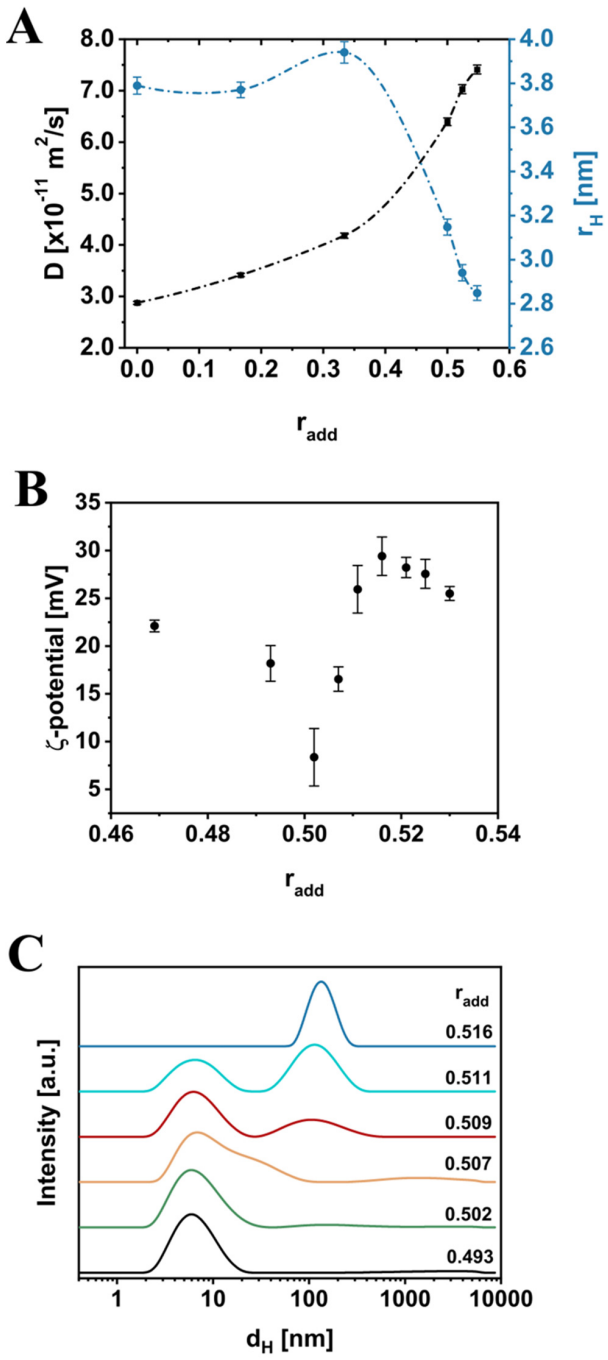

Figure 6. (**A**) The diffusion coefficients (black squares) of the PAH for different r_{add} were obtained by fitting the ^{1}H-PFG-STE NMR measurements. The hydrodynamic radii r_H (blue circles) were calculated using the Stokes–Einstein equation. The dotted lines are guides to the eyes. (**B**) ζ-potential measurements for different r_{add} show a minimum for r_{add} = 0.502. (**C**) The DLS measurements reaching different r_{add} were conducted 10 min after the phosphate addition was completed.

3.4. Macroscopic Ca^{2+}/PA Coacervate Gels

To identify possible application areas of the macroscopic, calcium-containing coacervate gels, their composition and properties must be elucidated first. Therefore, the concentration and pH ranges for the precipitation and isolation of macroscopic coacervates were investigated and summarized in a pseudo-phase diagram to determine the optimal synthesis conditions (Figure S10). Using a PA (19.5 kDa) solution at pH 9 (100 g/L), high yields of a homogeneous coacervate hydrogel were obtained, which were used for further investigations.

As described above, the calcium binding is dependent on the addition speed of the $CaCl_2$ solution, hence, an excess of Ca^{2+} was rapidly added to the PA solution within some seconds to maximize the calcium absorption. The synthesized coacervates were washed with water to remove the remaining unbound calcium ions as well as the chloride and sodium counterions of the initial PA-Na and $CaCl_2$ solution, respectively. Since the macroscopic coacervate is thermodynamically stable, the hydrogel can be dried and rehydrated any number of times. The calcium content of the coacervate reached up to 18.8 wt.%, which was calculated from the thermogravimetric analysis (TGA, Figure S11) and was further verified by energy-dispersive X-ray (EDX) spectroscopy (Figure S12, 19.2 wt.%). In addition, in the EDX spectrum, no impurities of chloride or sodium ions were detected, which proved a successful washing procedure. Moreover, the absence of impurities allows the assumption that the measured amount of calcium ions was bound and not entrapped; otherwise, they would also have been washed out. Therefore, a calcium amount of 18.8 wt.% can be expressed in a Ca^{2+}/COO^- ratio of 0.48, which is close to saturation. This high Ca^{2+} content is highly advantageous if the coacervates are applied as a calcium reservoir as will be investigated later. Complementary, the calcium-binding of the dried coacervate was assessed by attenuated total reflection Fourier transform infrared spectroscopy (ATR-FTIR, Figure S13). The downshift of the COO^--asymmetric stretching vibration (1532 cm^{-1}) of 40 cm^{-1} for the coacervate compared to the PA-Na (1572 cm^{-1}) elucidated calcium coordination by bidentate chelation of the calcium ions by four oxygen atoms of two acrylate groups [54,65].

For potential applications, not only the calcium content but also the rheological properties of the hydrogels are of ubiquitous interest. Hydrogels with a pronounced liquid behavior are desired for use as infiltrates, whereas higher plasticity is needed for use as mechanically more robust compounds. While investigating the factors influencing the rheological parameters (viscosity η, storage, and loss modulus G' and G'') of the coacervate gels, two factors, in particular, played major roles: the molecular weight of the PA reported in one of our recent publications [46] and the amount of calcium added identified in this study. To unravel the role of molecular weight, two Ca^{2+}/PA coacervates with distinct M_W (19.5 and 119 kDa, GPC in Figure S14) were synthesized, and their resultant rheology was analyzed (Figure 7A,B). The PA concentration, the pH values of the solutions, and the added amount of $CaCl_2$ for both systems were kept the same. For both coacervates, the viscoelasticity alters substantially with the frequency, which can be explained by the physical crosslinking [66]. Moreover, for the low molecular weight coacervate (LMC, red), the G' is lower than G'', indicating a dominant role of the viscosity. For the high molecular weight coacervate (HMC, green) the viscoelasticity also displayed a frequency-dependent behavior but the values for G' and G'' are 100 times higher than for the LMC. The loss modulus of the HMC exhibits a marginally higher value than G', which indicates only a slightly dominant role of the viscosity and a more plastic behavior than the LMC [46]. The moduli for the HMC (up to 10^5 Pa) are remarkably high compared to other typical hydrogels (<1000 Pa) [67] and are in good agreement with investigations for comparable systems [46,68]. Moreover, the viscosity of the HMC is 2–50 times higher than that of LMC (dependent on the frequency) and exhibits a strong shear-thinning behavior, whereas the viscosity of the LMC is almost independent of the frequency (Figure 7B). In brief, the rheological investigations presented here explain the plasticity and shapeable properties of the HMC [68], whereas the LMC shows a more liquid character.

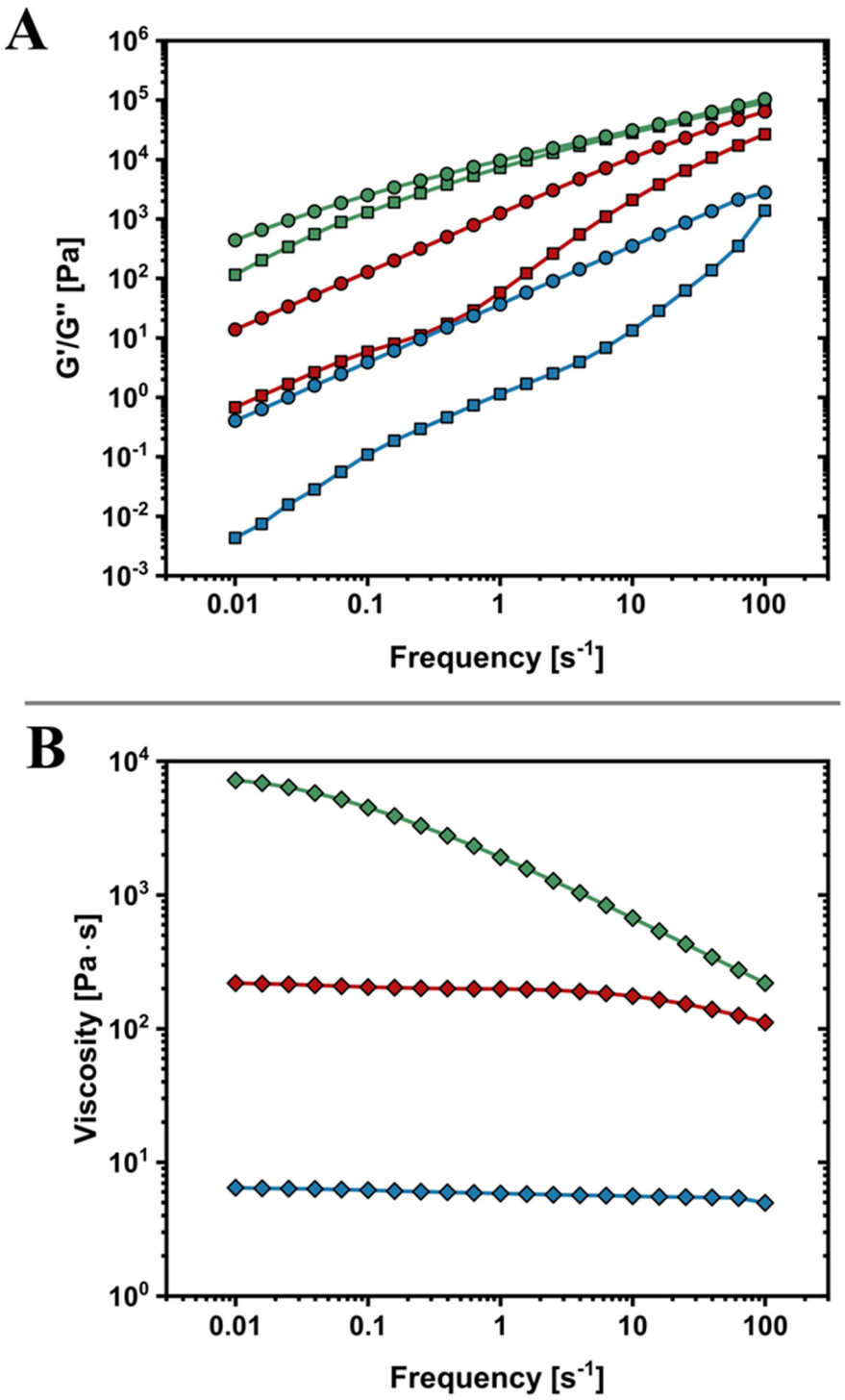

Figure 7. (**A**) Measurements of the storage (G′, squares) and loss (G″, circles) moduli of the high molecular weight coacervate (HMC, green), the low molecular weight coacervate (LMC, red) and the lowest ratio coacervate (LRC, blue) were frequency dependent. (**B**) Frequency-dependent viscosity measurements of the three coacervates (HMC-green, LMC-red and LRC-blue).

The significant differences in the rheological properties of HMC and LMC could be due to the different calcium content. As reported before, the complexation of calcium ions depends on the PA's molecular weight, whereas PAs with higher molecular weight could coordinate a higher Ca^{2+} amount [39,46,54]. Unexpectedly, the TGA of the HMC elucidated a negligibly higher calcium content of 19.4 wt.% (Figure S15). Hence, the rheological differences could emerge from the capability of more entanglements and a more efficient

intermolecular crosslinking for higher M_W PA compared with the LMC [46]. In addition, the calcium binding of PA is known to be stronger for higher M_W PA [54], which could result in a tougher network. Fuhrer et al. proposed that shorter PA chains act as plasticizers, whereas higher M_W PA chains built the hydrogel network [46]. For the HMC, the amount of shorter chains was lower, which could lead to a higher viscosity and tougher hydrogels reflected in higher values of G′ and G″.

The second influential factor affecting the rheological properties of the hydrogels is the volume of the added $CaCl_2$ solution. The images in Figure S16 illustrate the different viscosities depending on the added Ca^{2+} amount to the same PA solution (19.5 kDa). The coacervate with the most fluid character was synthesized by adding $CaCl_2$ to reach a ratio of 0.376, which is very close to the phase boundary (0.375) determined above for the droplet formation. The proximity to the phase boundary denied a washing procedure with water, as the coacervate would dissolve due to the high osmotic pressure. When a r_{add} of 0.423 was reached, the coacervate gel was stable in water. The product with the lowest ratio (0.376, LRC) was investigated by rheological analysis (blue, Figure 7A,B) and compared to the coacervate with the highest ratio (0.627). For clarity, the latter coacervate with the highest ratio is the same as described above and named LMC. The general course of the measured moduli of the LRC was comparable to the ones determined for the LMC, indicating a more dominant role of viscosity again. Furthermore, the viscosity was almost independent of the applied frequency and three times lower than the LMC.

The calcium content of the LRC was determined by TGA (Figure S17A) and amounted to 20.7 wt.%, corresponding to a slightly oversaturated Ca^{2+}/COO^- ratio of 0.507. This value was too high to reflect the bound calcium ratio. If the added calcium had been bound quantitatively, the mass fraction of Ca^{2+} would have been 17.5 wt.%. This excess of calcium or impurities elucidated by TGA could result from the unfeasibility of washing this coacervate due to its proximity to the phase boundary. On this account, residual sodium and a small amount of chloride ions were detected by EDX and amounted to 4.5 wt.% in total (Figure S17B). These impurities were not considered in the calculations of the calcium content based on TGA results, wherefore the actual Ca^{2+} content was lower. Furthermore, the impurities suggest that a fraction of the detected Ca^{2+} did not crosslink the PA by chelating but was entrapped or coordinated by another not-crosslinking binding mechanism [54]. The lower viscosity and moduli of the LRC could also be highly affected by the water content. Confocal Raman microscopy was used to compare the relative water content inside the coacervates independently from the surface-bound water (Figure S18). The relative water fractions of four different coacervates ($0.376 \leq r_{add} \leq 0.627$) were estimated by measuring the water-related CCD counts in the coacervate and in the supernatant (Figure S18D). These measurements confirmed a 10% higher water content for the LRC than for the LMC, which could have a decisive influence on the rheological properties. The combination of a higher water content in the coacervate and a lower calcium content crosslinking the polymer chains is presumed to be the reason for the vast differences in the rheological behavior of the coacervate gels [3].

3.5. Applications

By varying the molecular weight of the PA and the added calcium content, it is possible to synthesize coacervates whose viscosity covers three orders of magnitude. On the one hand, the hydrogels with fluidic character can be injected using a standard syringe (Figure 8A) or infiltrate cavities and cracks, which is highly advantageous regarding their application in confined spaces. Those coacervates could also be spin-coated to prepare thin and transparent coacervate layers. On the other hand, the highly viscous coacervates show more plastic and shapeable properties, which could be interesting for developing sustainable plastic materials [66]. Furthermore, the coacervates exhibit strong stretchability (Figure 8B) and fast self-healing within several seconds (Figure 8C). The self-healing properties are based on the highly dynamic calcium coordination, which were initially investigated by ^{1}H-NMR studies above. Those properties are very beneficial to achieve

a longer operational cycle of the hydrogels. In addition, the Ca^{2+}/PA coacervates have a high density of acidic groups, which can bind to several surfaces and act as adhesives. As a proof of concept, it was possible to glue two mussel shells strongly by using the well-described LMC as an adhesive (Figure 8D). Li et al. described the high adhesive strength of comparable polyacrylate-based hydrogels with an interlocking model; therefore, a viscous character of the hydrogel is preferred to increase the covered surface of the substrate and, therefore, the adhesion [6].

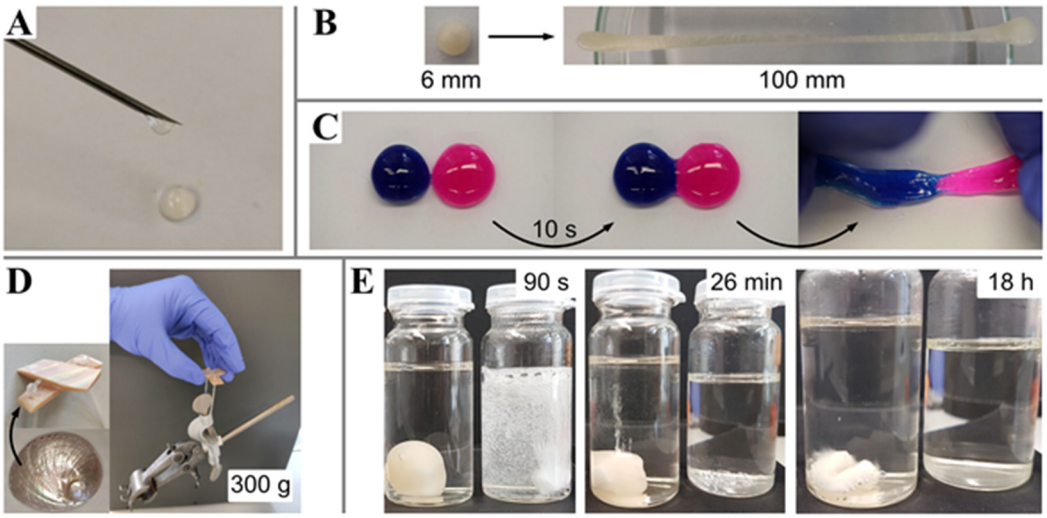

Figure 8. (**A**) Image demonstrates the injectability of the LRC using a normal syringe needle. (**B**) Photos of a small piece of LMC, which was stretched by a factor of 17 without breaking. (**C**) The LMCs were colored by introducing dyes (rhodamine B and methylene blue) to present the self-healing within some seconds. (**D**) The LMC was used as an adhesive to glue two pieces of a mussel shell (red abalone, inset), which could lift a stand clamp (~300 g) without breaking. (**E**) Images of the time-dependent dissolution of pure marble (right glasses) and marble which was wrapped by the LMC (left glasses) in a 12 M HCl solution.

Moreover, the coacervates obtained in this study possess astonishing protective properties. The LMC, for example, is insoluble in alkaline aqueous solutions and comparatively stable even in highly acidic environments. For illustration, a piece of marble was enveloped by the LMC and placed in a highly acidic solution (12 M HCl, Figure 8E). A piece of pure, unprotected marble was used as a reference, which immediately started to dissolve. The dissolution of the pure marble was completed after 10 min whereas the coacervate-protected marble was completely stable for more than 20 min. After 26 min, the first bubble formation was observed, indicating the dissolution of the marble and subsequent CO_2 release. After 18 h, the marble coated with the coacervate still did not completely dissolve. We envisage that the stability of coacervates in acidic media bears on the high calcium binding. To dissolve the coacervate, the acrylate groups must be protonated to break up the Ca^{2+}-crosslinks of the PA chains. The protonation of the acrylate groups simultaneously means a reduction in the free proton concentration and, thus, a partly neutralization near the coacervate surface. The stability against acidic solutions, in combination with the adhesion, plasticity, and self-healing properties, hold high potential for applications in anti-corrosion protection. In addition, the ambit of these coacervates is not only limited to aqueous solutions. They are also insoluble in polar organic solvents such as methanol, ethanol, or nitromethane as well as in non-polar solvents like toluene, 1,4-dioxane, or chloroform (results not shown).

The usage of coacervates as adhesive, flexible, and chemically resistant components is only one of several potential fields of application. In a second approach, the high calcium content of the coacervates can be exploited by using it as a calcium reservoir for further reactions. For this purpose, the injectable as well as the plastic coacervates could be

used as highly appropriate ions reservoir for the formation of crystalline calcium bearing phases such as calcium carbonates. By adding a carbonate solution to the coacervate (LMC), Ca^{2+} ions were bound by the (bi)carbonate ions to form calcite and vaterite phases (Figure 9A,B). Due to the comparable binding behavior of (bi)carbonate and acrylate to Ca^{2+} ions, the crystallization of a thick $CaCO_3$ layer takes a rather long period of time (up to several weeks).

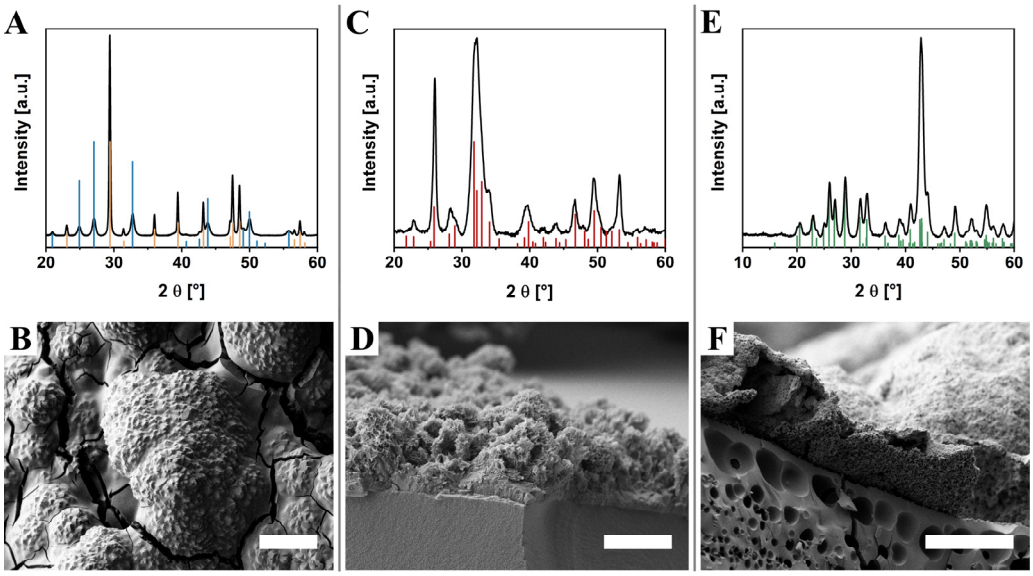

Figure 9. (**A**) Powder X-ray diffraction pattern of a coacervate (LMC) treated by carbonate solution shows the crystallization of mainly calcite (beige, PDF 47-1743) and a small amount of vaterite (blue, PDF 33-0268) phases. (**B**) The SEM image displays the polycrystalline aggregates of calcite (scale bar: 20 µm). (**C**) The powder X-ray diffraction pattern proves the crystallization of hydroxyapatite (red, PDF 85-3476). (**D**) The crystallization took place at the coacervate surface (LMC), which is indicated by the dense HAP layer on top of the coacervate (cross-section SEM image, scale bar: 5 µm). (**E**) The powder X-ray diffraction pattern shows the crystallization of barite ($BaSO_4$) by using a Ba^{2+}/PA coacervate (green, PDF 80-0512). (**F**) The cross-sectional SEM image displays a thick and dense barite layer built out of small crystals on top of the coacervate, the latter exhibits a typical porosity of dried hydrogels (scale bar: 50 µm).

The relatively long crystallization times are most likely also caused by the PA chains liberated from the coacervate to the solution, which could hinder the nucleation and crystal growth of crystalline phases of $CaCO_3$ since PA is well-known as a scale inhibitor [69].

The capability of the coacervate to induce the formation of inorganic phases could also be expanded to calcium phosphate systems whereas a formation of nano-crystalline hydroxyapatite (HAP) [70] was achieved (Figure 9C). The crystallization occurred exclusively at the coacervate surface, which was reflected in the formation of a dense apatite layer (several microns within 14 d) on top of the coacervate (Figure 9D). We assume that the (hydrogen)phosphate ions could not penetrate the coacervate due to the electrostatic interactions of the negatively charged (hydrogen)phosphate ions and PA chains. Therefore, the Ca^{2+} ions were released from the coacervate, because of the high binding affinity of phosphate to calcium ions, and resulted in a HAP crystallization at the surface. Those systems could be highly beneficial for the biomimetic mineralization of bones or dental hard tissue. In one possible scenario, the coacervate could be introduced into tooth lesions or cavities and mineralized due to the high phosphate content in saliva. In addition, PA is known to be a very good adhesive for dental cements [71]. Transitions in pH and ionic compositions during mineralization can also affect the plasticity of the hydrogel, as previously demonstrated for organic coacervates [72]. The plasticity and infiltration capability,

combined with the adhesive properties and the opportunity of bioinspired crystallization opens a new application sector of those coacervates in dentistry and osteology.

In general, the reported coacervation mechanism is not restricted to calcium ions. As reported by Schupp et al., the complex coacervation with PA can be amplified to a variety of bivalent metal ions resulting in macroscopic hydrogels [68]. For example, by using barium chloride, a Ba^{2+}/PA coacervate was synthesized with a barium content of 48 wt.% (measured by EDX, Figure S19). These coacervates were reacted with a sulfate-bearing solution and built within one hour to a thick $BaSO_4$ (barite) layer (~50 µm) on top of the coacervate (Figure 9E,F). The crystallization was much faster compared to the calcium-based systems, which could be related to the different binding behavior of Ba^{2+} to PA [42,73], as well as to the high binding affinity of Ba^{2+} to sulfate ions. The coacervates presented here could act as a new class of stable ions reservoir for a precipitation of inorganic phases and the formation of composite materials with simultaneously exceptional properties [3].

4. Conclusions

In conclusion, in the first part of this study we investigated the intricate formation mechanism of calcium-containing complex coacervates (Figure 5). For PA-Ca^{2+}, the entropically driven calcium coordination is highly dynamic, and this most likely enables the coalescence and fusion of coacervate droplets due to intermolecular crosslinking. By using ^{1}H-PFG-STE NMR coupled with DLS, ζ-potential, and potentiometric titration measurements, we unravel the different stages of calcium coordination and the conformational changes, which finally result in complex coacervation. First, the calcium ions were coordinated intramolecularly, which led to a screening of the negative charges of the polyelectrolyte and induced a coil-to-globular transition. Those globular Ca-PA chains precipitated due to coalescence and intermolecular crosslinking when the determined phase boundary was crossed, yielding a coacervate nanodroplet phase, which was electrostatically stabilized. The coacervate droplets of the emulsion showed tunable stability, which is a weighty factor for the possible usage as infiltrates in confined environments. The coacervate droplets grow and lastly fused to form a macroscopic coacervate hydrogel. Furthermore, we were able to decipher the mechanism of a cationic system (PO_4^{3-}/PAH coacervates) and draw striking parallels between the contrasting systems, although the initial driving force for polymer–ion complexation was different.

The calcium-containing hydrogels obtained in this study displayed a wide variety of promising properties such as self-healing, stretchability, adhesion, and resistance against alkaline and acidic environments, as well as many organic solvents, which opens a broad field of possible applications. Furthermore, by a simple variation in the synthesis route, the rheological properties of those coacervates could be tuned to bridge three orders of magnitude in viscosity. Thereby, injectable liquid-like hydrogels, as well as more plastic and shapeable coacervates, were accessible. In addition, we showed that the coacervation and reactivity of the hydrogels are extendable to a broad range of solid (crystalline) phases, like barium sulfate, calcium carbonate and phosphate. The gained knowledge of the dynamic calcium coordination to PA, the resulting conformation changes, and the precipitation mechanism decisively affect the properties of the macroscopic coacervates and open a plurality of possible applications, like water-based corrosion protection or adhesives. On top of that, the high calcium content of these hydrogels opens up the possibility to use those coacervates as a calcium reservoir for the formation of calcium carbonate and phosphate. This promising ability, combined with the strong adhesion to biomineral surfaces and the acid stability, creates a high potential for new bioinspired materials for dentistry and osteology applications.

Supplementary Materials: The following supporting information can be downloaded at https://www.mdpi.com/article/10.3390/cryst14110959/s1, Additional Experimental Results [51]; Figure S1: (A) Results of an exemplary potentiometric pH titration of a PA-Na solution (208 µmol) with NaOH (100 mM) for the investigation of the pKa of the PA. The pKa was calculated by the first turning point of the curve and was determined to be 4.28. (B) Gel permeation chromatography (GPC) measurement

of the mainly used PA-Na ($M_W \approx 15$ kDa, supplier info) shows a broad molecular weight distribution with a polydispersity index (PDI) of 4.9 and M_W = 19.5 kDa. The black curve displays the results of the refractive index detector, whereas the red curve shows the result of the UV detector (260 nm). The vertical line at 500 g/mol indicates the lower limit of the measurement. Figure S2: Isothermal titration calorimetry (ITC) raw (A) and integrated (B) curves for the Ca^{2+} complexation by PA. A $CaCl_2$ solution (270 µL, 4 mM, pH9) was titrated to 1.4 mL of a PA-Na solution (50 mg/mL, pH 9, borate buffered). The molar ratio is between the calcium ions and the acrylate subunits of the polymer. The data indicate an endothermic complexation reaction. Figure S3: ^{13}C-NMR spectra of the carboxylic groups of pure polyacrylate sodium salt and for the different Ca^{2+}/COO^- ratios (r_{add}). The line shape of the carboxylic carbon changed as soon as r_{add} was increased. Furthermore, the broad signals of the carboxylic carbon of the acrylate subunits shifted to higher chemical shifts with increasing r_{add}. The measurements were referenced to the carboxylic carbon of deuterated TMSPA (3-(trimethylsilyl)propionic acid sodium salt, δ = 185.76 ppm). Figure S4: (A) Results of a potentiometric titration experiment for the addition of a $CaCl_2$ solution (50 mM) with a constant addition rate (1 mL/min) until a ratio of r_{add} = 0.387 was reached (n(PA) = 4.24 mmol). The added calcium amount (red), the pH (green), the transmittance (black), and the free calcium (blue) was measured in situ and plotted against the time. (B) Zoom-in the first 11 ks of the measurement in (A). (C) Potentiometric titration measurement (inset: zoom-in) of bound Ca^{2+} ions (solid line) plotted against the added calcium. The dotted line displays the theoretical curve for a complete calcium binding. The first deviation of the measured value from the theoretical value was detected at a ratio of 0.187, indicating the maximum ratio of complete calcium complexation by PA. Note that the saturation of the PA by Ca^{2+} could not be reached due to the induced phase separation. (A 50 mM $CaCl_2$ solution was titrated to 4.24 mmol PA). Figure S5: (A) One exemplary DLS measurement which was performed directly after the calcium addition (r_{add} = 0.387) was completed, indicating one distinct droplet species with an average d_H of 210 nm. (B) Time-dependent DLS measurements after the addition of Ca^{2+} to reach a final ratio of r_{add} = 0.387 displays the growth of the droplets during several hours. After 17 h the bigger droplets coalesced and sedimented (sticky precipitate at the bottom of the vessel), wherefore only the smaller droplets remained in the emulsion. Figure S6: The emulsion stability for different synthesis parameters is shown in dependency of the r_{add}, the addition rate, and whether the sample was stirred (indicated as 'stir') after the addition was completed or not (indicated as 'stop'). The closer the r_{add} reached to the critical ratio of the phase separation (0.375), the more stable the emulsion was. Furthermore, not stirring increased the stability by a factor of 2, whereas the addition rate did not play a significant role. The stability was defined as the time for which the transmittance was lower than 50 mV. The samples for lower r_{add} (0.377 and 0.375) stayed slightly turbid for several days but the value of the transmittance did not reach the 50 mV border (Figures 3A and S7A), therefore, those samples are not included in this figure. Figure S7: (A) Results of a potentiometric titration experiment for the addition of a $CaCl_2$ solution (50 mM) to a PA solution (4.24 mmol) with a constant addition rate (1 mL/min) until a ratio of r_{add} = 0.377 was reached. The added calcium, the pH, the transmittance, and the free calcium were monitored in situ and plotted against the time. (B) DLS measurements of the sample shown in (A) directly after the addition was completed (black) show a major initial small species with d_H of 6–7 nm, which vanished within the first 16 min (last measurement: blue), whereas a second, larger species appeared and grew from 145 to 250 nm during the same time. Figure S8: ITC raw (A) and integrated (B) curves for the phosphate binding by PAH. A $(NH_4)_2HPO_4$ solution (270 µL, 5 mM, pH 7) was titrated to 1.4 mL of a PAH solution (50 mg/mL, pH 7, MOPS buffered). The molar ratio is the ratio between the phosphate anions and the amine subunits of the polymer. The exact values of the calculated thermodynamic parameters ($\Delta G = -26.9$ kJ/mol, $\Delta H = -20.8$ kJ/mol, $T\Delta S$=6.1 kJ/mol, T = 298 K) should be handled with care, since the fit is not perfectly fitting the measured data. Figure S9: Exemplary potentiometric pH titration of a PAH solution (213 µmol) with NaOH (100 mM, 0.1 mL/min) for the investigation of the pKa of the PAH. The first inflection point is due to the neutralization of excess HCl, which is needed for reaching the starting pH of 2. The pKa was calculated by the second inflection point of the curve and was determined to be 9.74. Figure S10: The pseudo phase diagram displays the concentration and pH regions for which the isolation of macroscopic coacervate hydrogels was possible (black squares in blue region, PA 15 kDa (supplier information)). The blue gradient indicates the yield of the resulting coacervate, which was higher for higher pH and PA concentration. The black lines are for illustration and are not exactly determined values. If the concentration of the PA was too low and/or the solution too acidic, either a turbid coacervate emulsion was obtained

(red squares) whereby the coacervate could not be isolated, or turbidity occurred (blue squares). Figure S11: (A) Thermogravimetric analysis (TGA) of the low molecular weight coacervate (LMC). The first decomposition step is due to residual water (finishing at about 250 °C) and most probably elimination reactions and rearrangements of the PA. The second sharp step (~450 °C) is according to the decomposition of the PA, resulting in calcium carbonate (plateau at 600 °C). The calcium carbonate decomposed to calcium oxide and released carbon dioxide (starting at 700 °C). Based on the final calcium oxide amount (800 °C), the initial Ca^{2+} content was calculated by using the ratio of molar masses (Ca^{2+}/CaO). (B) The product of the TGA at 600 °C was identified as calcite (green, PDF 47-1743) by applying X-ray diffraction (XRD). (C) XRD pattern of the residual product from TGA at 1000 °C. The product was mainly calcium oxide (red, PDF 37-1497), which slightly started to hydrolyze to calcium hydroxide (blue, PDF 44-1481) due to the humidity in air. Figure S12: EDX spectrum of the coacervate (LMC) proves the successful washing procedure due to the absence of sodium and chloride signals, which would be related to the educts (PA-Na and $CaCl_2$). The calcium content was determined to 19.2 wt.%. Figure S13: ATR-FTIR spectra of polyacrylic acid (black), PA-Na (red), and the Ca^{2+}/PA coacervate (19.5 kDa, blue) show a downshift of the COO^--asymmetric stretching vibrations (highlighted by the dotted lines) which is related to the different counterions (H^+, Na^+, Ca^{2+}). Figure S14: GPC measurement of the polyacrylic acid ($M_W \approx 100$ kDa, supplier info) used for the synthesis of the high molecular weight coacervate (HMC) shows a broad molecular weight distribution with a polydispersity index (PDI) of 8 and M_W = 119 kDa. The black curve displays the results of the refractive index detector, whereas the red curve shows the result of the UV detector (260 nm). The vertical line at 500 g/mol indicates the lower limit of the measurement. Figure S15: TGA measurement of the high molecular weight coacervate (HMC). The decomposition steps followed the same course as for the LMC (Figure S11A), indicating the decomposition of the PA of the HMC to $CaCO_3$ (600 °C), which, in turn, further decomposed to CaO (plateau at 1000 °C). Figure S16: Images of coacervates synthesized by the addition of different $CaCl_2$ volumes (200 mM) to the same amount of PA (M_W = 19.5 kDa, pH 9, 12.76 mmol, 100 g/L) to reach the final ratios (r_{add}) given below the images. The viscosity as well as the coacervate content increased with an increasing r_{add}. Figure S17: (A) TGA measurement of the lowest ratio coacervate (LRC) shows almost the same course as the LMC (Figure S11A) and the HMC (Figure S15) hinting to a similar sample composition. (B) EDX spectrum of the LRC shows residual impurities of mainly sodium from the PA-Na and chloride from the $CaCl_2$ solution (total content of 4.5 wt.%). The measurements were conducted using the coacervate as synthesized and without washing steps, which was due to the proximity to the phase boundary and therefore the instability in water. The calcium content was determined to be 13.1 wt.%. Figure S18: (A) Representative false color map of a freshly prepared coacervate sample (LMC) shows the coacervate phase (red), the supernatant (blue) and cover glass (green) acquired by using confocal Raman microscopy (scale: 20 μm). The scan area was perpendicular to the (B) image plane (scale: 40 μm). The projection of the scanned area is indicated by the dotted line. Maps were produced by using integral values for characteristic Raman peaks for silica (847–997 cm^{-1}, green), water (3100–3700 cm^{-1}, blue), and the polymer (2875–3025 cm^{-1}, red). (C) Representative spectra of silica (green), water (blue), and coacervate (red) were used for estimating the relative water contents. (D) For estimating the relative water fractions in coacervate (blue) and non-coacervate (red) phases, areas (white frames (A), 10×5 pixels) at equidistant distances from the cover glass interfaces were selected. The relative water fractions were determined at different areas for each r_{add} by normalizing the CCD counts of the water band (3100–3700 cm^{-1}) in the coacervate and in the supernatant. Figure S19: EDX spectrum of the Ba^{2+}/PA coacervate displays the successful washing procedure because no impurities of chloride (from $BaCl_2$) and sodium (from PA-Na) were detected. The barium content was determined to be 48 wt.%. Figure S20: (A) Image of an exemplary empty template used for the mineralization experiments. (B) Image of a template which is filled with the coacervate prior to use for the mineralization experiments. The coacervates were transparent. Table S1: Densities and viscosities were measured at 298 K with the Density Meter DMA 5000M (Anton Paar) equipped with a Microviscometer Louis 2000 ME (Anton Paar).

Author Contributions: Conceptualization, H.C. and E.V.S.; Data curation, D.G., C.R.-A., H.C. and E.V.S.; Formal analysis, A.R. and S.P.; Funding acquisition, H.C. and E.V.S.; Investigation, D.G., C.R.-A., A.R., S.P.; Methodology, D.G., C.R.-A., S.P., H.C. and E.V.S.; Project administration, H.C. and E.V.S.; Supervision, H.C. and E.V.S.; Visualization, D.G.; Writing—original draft, D.G.;

Writing—review and editing, D.G., C.R.-A., A.R., H.C. and E.V.S. All authors have read and agreed to the published version of the manuscript.

Funding: This research was funded by the DMG Dental-Material Gesellschaft mbH (Hamburg, Germany).

Data Availability Statement: The data presented in this study are available on request from the corresponding authors.

Acknowledgments: This manuscript is dedicated to our late colleague, mentor and former Editor in Chief of Crystals, Helmut Cölfen, who supervised this project and worked on this manuscript but unfortunately lost his fight against cancer on the 28 November 2023. The authors thank the DMG Dental-Material Gesellschaft mbH for financial support. We thank the laboratory of Bastiaan Staal from the BASF SE for the GPC measurements. In addition, we thank Anke Friemel and Michael Kovermann for the NMR experiments and results discussion, Ann-Kathrin Göppert for the TGA measurements, and Ulrich Bahnmüller for the synthesis of the barium coacervates. Moreover, the authors thank Holger Müller, Stephan Neffgen, and Olav-Sven Becker for discussions and suggestions regarding the coacervate applications. Furthermore, the authors thank the Deutsche Forschungsgemeinschaft for the framework of the Collaborative Research Center SFB-1214 "Anisotropic Particles as Building Blocks" and the included "Particle Analysis Center" (Project Z1) for the XRD, DLS and ζ-potential measurements. E.V.S and C.R.-A. thank the "Zukunftskolleg" (University of Konstanz) for financial support.

Conflicts of Interest: The authors declare no conflicts of interest.

References

1. Sun, J.-Y.; Zhao, X.; Illeperuma, W.R.K.; Chaudhuri, O.; Oh, K.H.; Mooney, D.J.; Vlassak, J.J.; Suo, Z. Highly stretchable and tough hydrogels. *Nature* **2012**, *489*, 133–136. [CrossRef] [PubMed]
2. Sun, T.L.; Kurokawa, T.; Kuroda, S.; Ihsan, A.B.; Akasaki, T.; Sato, K.; Haque, M.A.; Nakajima, T.; Gong, J.P. Physical hydrogels composed of polyampholytes demonstrate high toughness and viscoelasticity. *Nat. Mater.* **2013**, *12*, 932–937. [CrossRef]
3. Gruber, D. *Precursors for the Remineralization of Dental Hard Tissues [Doctoral Dissertation]*; University of Konstanz: Konstanz, Germany, 2020.
4. Gao, H.; Sun, Y.; Zhou, J.; Xu, R.; Duan, H. Mussel-Inspired Synthesis of Polydopamine-Functionalized Graphene Hydrogel as Reusable Adsorbents for Water Purification. *ACS Appl. Mater. Interfaces* **2013**, *5*, 425–432. [CrossRef]
5. Rao, P.; Sun, T.L.; Chen, L.; Takahashi, R.; Shinohara, G.; Guo, H.; King, D.R.; Kurokawa, T.; Gong, J.P. Tough Hydrogels with Fast, Strong, and Reversible Underwater Adhesion Based on a Multiscale Design. *Adv. Mater.* **2018**, *30*, 1801884. [CrossRef]
6. Li, A.; Jia, Y.; Sun, S.; Xu, Y.; Minsky, B.B.; Stuart, M.A.C.; Cölfen, H.; von Klitzing, R.; Guo, X. Mineral-Enhanced Polyacrylic Acid Hydrogel as an Oyster-Inspired Organic–Inorganic Hybrid Adhesive. *ACS Appl. Mater. Interfaces* **2018**, *10*, 10471–10479. [CrossRef]
7. Hoare, T.R.; Kohane, D.S. Hydrogels in drug delivery: Progress and challenges. *Polymer* **2008**, *49*, 1993–2007. [CrossRef]
8. Armstrong, J.P.K.; Puetzer, J.L.; Serio, A.; Guex, A.G.; Kapnisi, M.; Breant, A.; Zong, Y.; Assal, V.; Skaalure, S.C.; King, O.; et al. Engineering Anisotropic Muscle Tissue using Acoustic Cell Patterning. *Adv. Mater.* **2018**, *30*, 1802649. [CrossRef] [PubMed]
9. Lee, H.-p.; Gu, L.; Mooney, D.J.; Levenston, M.E.; Chaudhuri, O. Mechanical confinement regulates cartilage matrix formation by chondrocytes. *Nat. Mater.* **2017**, *16*, 1243–1251. [CrossRef]
10. Yu, L.; Ding, J. Injectable hydrogels as unique biomedical materials. *Chem. Soc. Rev.* **2008**, *37*, 1473–1481. [CrossRef]
11. Wang, W.; Zhang, Y.; Liu, W. Bioinspired fabrication of high strength hydrogels from non-covalent interactions. *Prog. Polym. Sci.* **2017**, *71*, 1–25. [CrossRef]
12. Guo, B.; Ma, P.X. Conducting Polymers for Tissue Engineering. *Biomacromolecules* **2018**, *19*, 1764–1782. [CrossRef] [PubMed]
13. Černý, J.; Hobza, P. Non-covalent interactions in biomacromolecules. *Phys. Chem. Chem. Phys.* **2007**, *9*, 5291–5303. [CrossRef]
14. Zhao, H.; Sun, C.; Stewart, R.J.; Waite, J.H. Cement Proteins of the Tube-building Polychaete Phragmatopoma californica. *J. Biol. Chem.* **2005**, *280*, 42938–42944. [CrossRef] [PubMed]
15. Stewart, R.J.; Wang, C.S.; Shao, H. Complex coacervates as a foundation for synthetic underwater adhesives. *Adv. Colloid Interface Sci.* **2011**, *167*, 85–93. [CrossRef]
16. de Kruif, C.G.; Weinbreck, F.; de Vries, R. Complex coacervation of proteins and anionic polysaccharides. *Curr. Opin. Colloid Interface Sci.* **2004**, *9*, 340–349. [CrossRef]
17. Kizilay, E.; Kayitmazer, A.B.; Dubin, P.L. Complexation and coacervation of polyelectrolytes with oppositely charged colloids. *Adv. Colloid Interface Sci.* **2011**, *167*, 24–37. [CrossRef] [PubMed]
18. Bungenberg de Jong, H.G.; Kruyt, H.R. Coacervation (Partial miscibility in colloid systems). *Proc. K. Ned. Akad. Wet.* **1929**, *32*, 849–856.
19. Schmitt, C.; Turgeon, S.L. Protein/polysaccharide complexes and coacervates in food systems. *Adv. Colloid Interface Sci.* **2011**, *167*, 63–70. [CrossRef]

20. Wang, B.; Adhikari, B.; Barrow, C.J. Optimisation of the microencapsulation of tuna oil in gelatin–sodium hexametaphosphate using complex coacervation. *Food Chem.* **2014**, *158*, 358–365. [CrossRef]
21. Mann, S. Systems of Creation: The Emergence of Life from Nonliving Matter. *Acc. Chem. Res.* **2012**, *45*, 2131–2141. [CrossRef]
22. Huang, X.; Li, M.; Green, D.C.; Williams, D.S.; Patil, A.J.; Mann, S. Interfacial assembly of protein–polymer nano-conjugates into stimulus-responsive biomimetic protocells. *Nat. Commun.* **2013**, *4*, 2239. [CrossRef] [PubMed]
23. Li, M.; Harbron, R.L.; Weaver, J.V.M.; Binks, B.P.; Mann, S. Electrostatically gated membrane permeability in inorganic protocells. *Nat. Chem.* **2013**, *5*, 529–536. [CrossRef]
24. Awada, H.K.; Johnson, N.R.; Wang, Y. Dual Delivery of Vascular Endothelial Growth Factor and Hepatocyte Growth Factor Coacervate Displays Strong Angiogenic Effects. *Macromol. Biosci.* **2014**, *14*, 679–686. [CrossRef] [PubMed]
25. Blocher, W.C.; Perry, S.L. Complex coacervate-based materials for biomedicine. *WIREs Nanomed. Nanobiotechnology* **2017**, *9*, e1442. [CrossRef]
26. Leong, K.W.; Mao, H.Q.; Truong-Le, V.L.; Roy, K.; Walsh, S.M.; August, J.T. DNA-polycation nanospheres as non-viral gene delivery vehicles. *J. Control. Release* **1998**, *53*, 183–193. [CrossRef]
27. de Silva, U.K.; Brown, J.L.; Lapitsky, Y. Poly(allylamine)/tripolyphosphate coacervates enable high loading and multiple-month release of weakly amphiphilic anionic drugs: An in vitro study with ibuprofen. *RSC Adv.* **2018**, *8*, 19409–19419. [CrossRef]
28. Huang, Y.; Lawrence, P.G.; Lapitsky, Y. Self-Assembly of Stiff, Adhesive and Self-Healing Gels from Common Polyelectrolytes. *Langmuir* **2014**, *30*, 7771–7777. [CrossRef]
29. Lawrence, P.G.; Patil, P.S.; Leipzig, N.D.; Lapitsky, Y. Ionically Cross-Linked Polymer Networks for the Multiple-Month Release of Small Molecules. *ACS Appl. Mater. Interfaces* **2016**, *8*, 4323–4335. [CrossRef] [PubMed]
30. Andreozzi, P.; Ricci, C.; Porcel, J.E.M.; Moretti, P.; Di Silvio, D.; Amenitsch, H.; Ortore, M.G.; Moya, S.E. Mechanistic study of the nucleation and conformational changes of polyamines in presence of phosphate ions. *J. Colloid Interface Sci.* **2019**, *543*, 335–342. [CrossRef]
31. Kanasty, R.; Dorkin, J.R.; Vegas, A.; Anderson, D. Delivery materials for siRNA therapeutics. *Nat. Mater.* **2013**, *12*, 967–977. [CrossRef]
32. Gruber, D.; Ruiz-Agudo, C.; Cölfen, H. Cationic Coacervates: Novel Phosphate Ionic Reservoir for the Mineralization of Calcium Phosphates. *ACS Biomater. Sci. Eng.* **2023**, *9*, 1791–1795. [CrossRef]
33. Lauth, V.; Maas, M.; Rezwan, K. Coacervate-directed synthesis of CaCO3 microcarriers for pH-responsive delivery of biomolecules. *J. Mater. Chem. B* **2014**, *2*, 7725–7731. [CrossRef] [PubMed]
34. Huang, S.-C.; Naka, K.; Chujo, Y. A Carbonate Controlled-Addition Method for Amorphous Calcium Carbonate Spheres Stabilized by Poly(acrylic acid)s. *Langmuir* **2007**, *23*, 12086–12095. [CrossRef] [PubMed]
35. Kaempfe, P.; Lauth, V.R.; Halfer, T.; Treccani, L.; Maas, M.; Rezwan, K. Micromolding of Calcium Carbonate Using a Bio-Inspired, Coacervation-Mediated Process. *J. Am. Ceram. Soc.* **2013**, *96*, 736–742. [CrossRef]
36. Kruyt, H.R. *Colloid Science, Volume II: Reversible Systems*; Elsevier Publishing Company: Amsterdam, The Netherlands, 1949.
37. Sinn, C.G.; Dimova, R.; Antonietti, M. Isothermal Titration Calorimetry of the Polyelectrolyte/Water Interaction and Binding of Ca^{2+}: Effects Determining the Quality of Polymeric Scale Inhibitors. *Macromolecules* **2004**, *37*, 3444–3450. [CrossRef]
38. Reith, D.; Müller, B.; Müller-Plathe, F.; Wiegand, S. How does the chain extension of poly (acrylic acid) scale in aqueous solution? A combined study with light scattering and computer simulation. *J. Chem. Phys.* **2002**, *116*, 9100–9106. [CrossRef]
39. Schweins, R.; Huber, K. Collapse of sodium polyacrylate chains in calcium salt solutions. *Eur. Phys. J. E* **2001**, *5*, 117–126. [CrossRef]
40. Huber, K. Calcium-induced shrinking of polyacrylate chains in aqueous solution. *J. Phys. Chem.* **1993**, *97*, 9825–9830. [CrossRef]
41. Schweins, R.; Lindner, P.; Huber, K. Calcium Induced Shrinking of NaPA Chains: A SANS Investigation of Single Chain Behavior. *Macromolecules* **2003**, *36*, 9564–9573. [CrossRef]
42. Schweins, R.; Goerigk, G.; Huber, K. Shrinking of anionic polyacrylate coils induced by Ca2+, Sr2+ and Ba2+: A combined light scattering and ASAXS study. *Eur. Phys. J. E -Soft Matter* **2006**, *21*, 99–110. [CrossRef]
43. Lages, S.; Lindner, P.; Sinha, P.; Kiriy, A.; Stamm, M.; Huber, K. Formation of Ca^{2+}-Induced Intermediate Necklace Structures of Polyacrylate Chains. *Macromolecules* **2009**, *42*, 4288–4299. [CrossRef]
44. Wang, P.; Yook, S.-W.; Jun, S.-H.; Li, Y.-L.; Kim, M.; Kim, H.-E.; Koh, Y.-H. Synthesis of nanoporous calcium phosphate spheres using poly(acrylic acid) as a structuring unit. *Mater. Lett.* **2009**, *63*, 1207–1209. [CrossRef]
45. McKenna, B.J.; Waite, J.H.; Stucky, G.D. Biomimetic Control of Calcite Morphology with Homopolyanions. *Cryst. Growth Des.* **2009**, *9*, 4335–4343. [CrossRef]
46. Fuhrer, L.M.; Sun, S.; Boyko, V.; Kellermeier, M.; Colfen, H. Tuning the properties of hydrogels made from poly(acrylic acid) and calcium salts. *Phys. Chem. Chem. Phys. PCCP* **2020**, *22*, 18631–18638. [CrossRef]
47. Berger, S.; Braun, S. *200 and More NMR Experiments: A Practical Course*, 3rd ed.; Wiley-VCH: Weinheim, Germany, 2004.
48. Stejskal, E.O.; Tanner, J.E. Spin Diffusion Measurements: Spin Echoes in the Presence of a Time-Dependent Field Gradient. *J. Chem. Phys.* **1965**, *42*, 288–292. [CrossRef]
49. Kuchel, P.W.; Pagès, G.; Nagashima, K.; Velan, S.; Vijayaragavan, V.; Nagarajan, V.; Chuang, K.H. Stejskal–tanner equation derived in full. *Concepts Magn. Reson. Part A* **2012**, *40A*, 205–214. [CrossRef]
50. Wiedenbeck, E.; Kovermann, M.; Gebauer, D.; Cölfen, H. Liquid Metastable Precursors of Ibuprofen as Aqueous Nucleation Intermediates. *Angew. Chem. Int. Ed.* **2019**, *58*, 19103–19109. [CrossRef] [PubMed]

51. Wang, T.; Cölfen, H. In Situ Investigation of Complex BaSO4 Fiber Generation in the Presence of Sodium Polyacrylate. 1. Kinetics and Solution Analysis. *Langmuir* **2006**, *22*, 8975–8985. [CrossRef]
52. Molnar, F.; Rieger, J. "Like-Charge Attraction" between Anionic Polyelectrolytes: Molecular Dynamics Simulations. *Langmuir* **2005**, *21*, 786–789. [CrossRef]
53. Mai, S.; Wei, C.-C.; Gu, L.-S.; Tian, F.-C.; Arola, D.D.; Chen, J.-H.; Jiao, Y.; Pashley, D.H.; Niu, L.-N.; Tay, F.R. Extrafibrillar collagen demineralization-based chelate-and-rinse technique bridges the gap between wet and dry dentin bonding. *Acta Biomater.* **2017**, *57*, 435–448. [CrossRef]
54. Fantinel, F.; Rieger, J.; Molnar, F.; Hübler, P. Complexation of Polyacrylates by Ca^{2+} Ions. Time-Resolved Studies Using Attenuated Total Reflectance Fourier Transform Infrared Dialysis Spectroscopy. *Langmuir* **2004**, *20*, 2539–2542. [CrossRef] [PubMed]
55. Verch, A.; Gebauer, D.; Antonietti, M.; Cölfen, H. How to control the scaling of CaCO3: A "fingerprinting technique" to classify additives. *Phys. Chem. Chem. Phys.* **2011**, *13*, 16811–16820. [CrossRef] [PubMed]
56. Gebauer, D. How Can Additives Control the Early Stages of Mineralisation? *Minerals* **2018**, *8*, 179. [CrossRef]
57. Lauth, V.; Loretz, B.; Lehr, C.-M.; Maas, M.; Rezwan, K. Self-Assembly and Shape Control of Hybrid Nanocarriers Based on Calcium Carbonate and Carbon Nanodots. *Chem. Mater.* **2016**, *28*, 3796–3803. [CrossRef]
58. Keckeis, P.; Drabinová, E.; Ruiz-Agudo, C.; Avaro, J.; Glatt, L.; Sedlák, M.; Cölfen, H. Multifunctional Block Copolymers for Simultaneous Solubilization of Poorly Water-Soluble Cholesterol and Hydroxyapatite Crystals. *Adv. Funct. Mater.* **2019**, *29*, 1808331. [CrossRef]
59. Bulo, R.E.; Donadio, D.; Laio, A.; Molnar, F.; Rieger, J.; Parrinello, M. "Site Binding" of Ca^{2+} Ions to Polyacrylates in Water: A Molecular Dynamics Study of Coiling and Aggregation. *Macromolecules* **2007**, *40*, 3437–3442. [CrossRef]
60. Lages, S.; Michels, R.; Huber, K. Coil-Collapse and Coil-Aggregation due to the Interaction of Cu^{2+} and Ca^{2+} Ions with Anionic Polyacylate Chains in Dilute Solution. *Macromolecules* **2010**, *43*, 3027–3035. [CrossRef]
61. Wilkins, D.K.; Grimshaw, S.B.; Receveur, V.; Dobson, C.M.; Jones, J.A.; Smith, L.J. Hydrodynamic Radii of Native and Denatured Proteins Measured by Pulse Field Gradient NMR Techniques. *Biochemistry* **1999**, *38*, 16424–16431. [CrossRef]
62. Swift, T.; Swanson, L.; Geoghegan, M.; Rimmer, S. The pH-responsive behaviour of poly(acrylic acid) in aqueous solution is dependent on molar mass. *Soft Matter* **2016**, *12*, 2542–2549. [CrossRef]
63. Ezhova, A.; Huber, K. Contraction and Coagulation of Spherical Polyelectrolyte Brushes in the Presence of Ag^{+}, Mg^{2+}, and Ca^{2+} Cations. *Macromolecules* **2016**, *49*, 7460–7468. [CrossRef]
64. Jachimska, B.; Jasiński, T.; Warszyński, P.; Adamczyk, Z. Conformations of poly(allylamine hydrochloride) in electrolyte solutions: Experimental measurements and theoretical modeling. *Colloids Surf. A Physicochem. Eng. Asp.* **2010**, *355*, 7–15. [CrossRef]
65. Nara, M.; Torii, H.; Tasumi, M. Correlation between the Vibrational Frequencies of the Carboxylate Group and the Types of Its Coordination to a Metal Ion: An ab Initio Molecular Orbital Study. *J. Phys. Chem.* **1996**, *100*, 19812–19817. [CrossRef]
66. Sun, S.; Mao, L.-B.; Lei, Z.; Yu, S.-H.; Cölfen, H. Hydrogels from Amorphous Calcium Carbonate and Polyacrylic Acid: Bio-Inspired Materials for "Mineral Plastics". *Angew. Chem. Int. Ed.* **2016**, *55*, 11765–11769. [CrossRef] [PubMed]
67. Bromberg, L.; Temchenko, M.; Alakhov, V.; Hatton, T.A. Bioadhesive properties and rheology of polyether-modified poly(acrylic acid) hydrogels. *Int. J. Pharm.* **2004**, *282*, 45–60. [CrossRef]
68. Schupp, D.J.; Zhang, X.; Sun, S.; Cölfen, H. Mineral plastic hydrogels from the cross-linking of polyacrylic acid and alkaline earth or transition metal ions. *Chem. Commun.* **2019**, *55*, 4913–4916. [CrossRef]
69. Gebauer, D.; Cölfen, H.; Verch, A.; Antonietti, M. The Multiple Roles of Additives in CaCO3 Crystallization: A Quantitative Case Study. *Adv. Mater.* **2009**, *21*, 435–439. [CrossRef]
70. Drouet, C. Apatite Formation: Why It May Not Work as Planned, and How to Conclusively Identify Apatite Compounds. *BioMed Res. Int.* **2013**, *12*, 1–12. [CrossRef]
71. Solhi, L.; Atai, M.; Nodehi, A.; Imani, M.; Ghaemi, A.; Khosravi, K. Poly(acrylic acid) grafted montmorillonite as novel fillers for dental adhesives: Synthesis, characterization and properties of the adhesive. *Dent. Mater.* **2012**, *28*, 369–377. [CrossRef]
72. Rao, A.; Cölfen, H. Mineralization and non-ideality: On nature's foundry. *Biophys. Rev.* **2016**, *8*, 309–329. [CrossRef]
73. Pochard, I.; Foissy, A.; Couchot, P. Conductometric and microcalorimetric analysis of the alkaline-earth/alkali-metal ion exchange onto polyacrylic acid. *Colloid Polym. Sci.* **1999**, *277*, 818–826. [CrossRef]